NEXT GENERATION PEM ELECTROLYSERS UNDER NEW EXTREMES

HORIZON 2020 PROGRAMME
FUEL CELLS AND HYDROGEN JOINT UNDERTAKING (FCH 2 JU)
Grant agreement no.: 779540
Start date: 01.02.2018 – **Duration**: 36 months
Project Coordinator: Catherine McDougall - ITM

DELIVERABLE REPORT

D4.1 – DATA-SET ON CATALYTIC ACTIVITY, ELECTROCHEMICAL PERFORMANCE AND STABILITY OF ENHANCED CATALYSTS		
Due Date	31-January-2019	
Authors	S. Siracusano, N. Briguglio, F. Pantò, G. Bonura, C. Busacca, A. Di Blasi, V. Antonucci, C. Lo Vecchio, V. Baglio, G. Monforte, S. Trocino, M. Girolamo, A.S. Aricò (CNR-ITAE) D. Greenhalgh (ITM) C. Oldani, M. Infantino, S. Tonella (SOLVAY) L. Grahl-Madsen (IRD)	
Workpackage	WP4	
Workpackage Leader	4 - CNR	
Lead Beneficiary	4 - CNR	
Date released by WP leader	21 January 2019	
Date released by coordinator	21 January 2019	
DISSEMINATION LEVEL		
PU	Public	**X**
PP	Restricted to other programme participants (including the Commission Services)	
RE	Restricted to a group specified by the consortium (including the Commission Services)	
CO	Confidential, only for members of the consortium (including the Commission Services)	
NATURE OF THE DELIVERABLE		
R	Report	**X**
D	Demonstrator	

O	Other	

SUMMARY	
Keywords	Electrolysis, Polymer electrolyte membranes, Electro-Catalysts, MEAs, Characterisation, Stack, System, Balance-of-plant, Procedures, Protocols
Abstract	The purpose of this Deliverable was to develop enhanced PEM electrolysis components characterised by a significant decrease of the noble metal content and an increase of the current density with respect to the state-of-the art. Membrane-electrode assemblies (MEAs) based on a novel Aquivion® membrane, specifically designed for water electrolysis, with enhanced $Ir_{0.7}Ru_{0.3}O_x$, Pt/C and Pt-Alloy catalysts have thus been developed and assessed in this work in terms of performance and durability using low catalyst loadings. In this deliverable, we are operating the MEAs at an electrolysis current density (4 A·cm^{-2}) in accordance with the project targets in the presence of a significant reduction of the total noble metal loading (0.44 mg·cm^{-2} MEA) while maintaining a very high conversion efficiency (>80%). The specific activity are thus addressed to: - The development of oxygen evolution electro-catalysts. The main approach of this task regards the improvement of the intrinsic activity and stability through tailoring anode catalyst surface chemistry, electronic effects and crystallographic orientation. The aim is to produce stable nanostructured solid solutions of Ir and Ru with a core-shell configuration consisting of Ir enrichment on the surface and optimised crystallographic orientation. • The development of hydrogen evolution electro-catalysts. As for the anode catalyst, noble metal-based cathode catalysts are necessary to provide corrosion resistance in acidic environment and appropriate catalytic activity for hydrogen evolution. These are essentially based on Pt. The aim of this task is to further reduce the cathode catalyst loading to less than 0.1-0.05 mg cm^{-2}, increase current density up to 4-8 A cm^{-2} while keeping the low overpotential characteristics of the hydrogen evolution process. Pt electrocatalysts for cathodic operation will be supported on a stable carbon nanofibres support to substitute microporous carbon blacks. • The development of anode integrated recombination catalyst. This task is addressing the development of an unsupported recombination catalyst based on a Pt-alloy with core-shell structure. A thin layer recombination catalyst, with ultralow PGM loading, will be integrated in the anode structure at the interface with the membrane to electrochemically oxidize permeated hydrogen that has not recombined inside the membrane. The aim is to limit the hydrogen content in the oxygen stream below a limit of 0.2-0.5% at high differential pressures (100 bar) through a dual layer recombination process.
Public abstract for confidential deliverables	N.A. - Public Deliverable

REVISIONS			
Version	**Date**	**Changed by**	**Comments**
0.1	21-01-2019	Antonino Aricò (CNR)	First draft
0.2	22-01-2019	Laila Grahl-Madsen (IRD)	Implementation
0.2	28-01-2019	Daniel Greenhalgh (ITM)	Implementation
0.5	29-01-2019	Antonino Aricò (CNR)	Final draft

Disclaimer/ Acknowledgment

Copyright ©, all rights reserved. This document or any part thereof may not be made public or disclosed, copied or otherwise reproduced or used in any form or by any means, without prior permission in writing from the NEPTUNE Consortium. Neither the NEPTUNE Consortium nor any of its members, their officers, employees or agents shall be liable or responsible, in negligence or otherwise, for any loss, damage or expense whatever sustained by any person as a result of the use, in any manner or form, of any knowledge, information or data contained in this document, or due to any inaccuracy, omission or error therein contained.
All Intellectual Property Rights, know-how and information provided by and/or arising from this document, such as designs, documentation, as well as preparatory material in that regard, is and shall remain the exclusive property of the NEPTUNE Consortium and any of its members or its licensors. Nothing contained in this document shall give, or shall be construed as giving, any right, title, ownership, interest, license or any other right in or to any IP, know-how and information.

This project has received funding from the FCH JU and European Union's Horizon 2020 research and innovation programme under grant agreement No 700008. This Joint Undertaking receives support from the European Union's Horizon 2020 research and innovation programme and Hydrogen Europe, and Hydrogen Europe Research

The information and views set out in this publication does not necessarily reflect the official opinion of the European Commission. Neither the European Union institutions and bodies nor any person acting on their behalf, may be held responsible for the use, which may be made of the information contained therein.

D4.1 – DATA-SET ON CATALYTIC ACTIVITY, ELECTROCHEMICAL PERFORMANCE AND STABILITY OF ENHANCED CATALYSTS

SUMMARY

1. INTRODUCTION……6

2. ENHANCED CATALYSTS PREPARATION……8

2.1 Anode Electrocatalyst……8

2.2.1 Physico-chemical properties of Anode catalyst……8

2.2 Cathode Electrocatalyst……12

2.2.1 Sulphite complex route……13

2.2.2 Catalytic decomposition method……13

2.2.3 Electrospinning……14

3. CATALYTIC ACTIVITY, ELECTROCHEMICAL PERFORMANCE AND STABILITY OF ENHANCED CATALYSTS……16

3.1 MEAs Characterization……17

4. ANODE INTEGRATED RECOMBINATION CATALYST……23

4.1 Experimental……23

4.2 Result and discussion……27

4.2.1 Structural and chemical characterisation of the Pt-based recombination catalysts……27

4.2.2 Assessment of the Pt-based catalysts for the hydrogen oxidation/ recombination in the gas-phase……31

4.2.3 Surface characterisation of the Pt-based catalysts……35

4.2.4 Single cell electrochemical assessment of a Pt-Co alloy for the hydrogen oxidation at the anode compartment of a PEM electrolysis cell……38

5. ELECTROCATALYSTS MEETING THE SPECIFICATIONS: ASSESSMENT OF PROJECT MILESTONE MS3 …..48

6. CONCLUSIONS……52

LIST OF ACRONYMS, ABBREVIATIONS AND DEFINITIONS

Acronym table

Abbreviation	Explanation
ADF	Amsterdam Density Functional
BET	Brunauer–Emmett–Teller
BF	Bright Field
CCM	Catalyst Coated Membrane
CL	Catalyst Layer
CNT	Carbon NanoTubes
DMF	DiMethylFormamide
ECSA	Electro Chemical Surface Area
EDX	Energy-dispersive X-ray spectroscopy
EIS	Electrochemical Impedance Spectroscopy
EW	Equivalent Weight
FC	Fuel Cell
FRA	Frequency Response Analyser
GDL	Gas Diffusion Layer
MEA	Membrane Electrode Assembly
PAN	PolyAcryloNitrile
PEM	Proton Exchange Membrane
PFSA	PerFluoroSulfonic Acid
SEM	Scanning Electron Microscope
STEM	Scanning Transmission Electron Microscope
TEM	Transmission Electron Microscopy
TGA	ThermoGravimetric Analysis
XPS	X-ray photoelectron spectroscopy
XRD	X-ray diffraction

1. INTRODUCTION

The main challenges to overcome for an effective, wide-scale, utilisation of hydrogen as energy carrier, regard both technical bottlenecks and an optimization of the energy cycle from renewable energy sources to end use via hydrogen generation, storage, transport, conversion and consumption. Technical problems are primarily dealing with the storage of hydrogen at high volumetric energy density, using low-energy consumption and cost-effective technologies characterised by intrinsic safety. Next generation water electrolysers are expected to operate at high pressure to reduce the efficiency losses in the gas post-compression step while offering proper dynamic behaviour in terms of rapid response and partial load operation. Generally, most of the present pressurised polymer electrolyte (PEM) electrolysers cannot operate at a partial load below 20% because of the excessive concentration of hydrogen in the oxygen stream at the anode at low current densities. The flammability limit of the H_2 concentration in O_2 is 4% vol. but for safety reasons the systems are shutdown when this concentration exceeds 2-3% vol.

Specific improvements of PEM electrolysers are required especially in terms of significant increase in current density, resulting in the proportional decrease in capital costs, whilst maintaining cutting edge efficiency in combination with a material use minimisation approach. This regards a reduced membrane thickness whilst keeping low the gas crossover and reducing the precious metal loading. For a PEM electrolyser operating at high current density, the role of the membrane is dominant in determining voltage efficiency and reaction rate. At high current density, the proton transport inside the membrane causes the largest contribution to the overall differential resistance. On the contrary, the polarisation resistance, for both anode and cathode processes decreases significantly when the overpotential is increased. Advanced PEM electrolysis systems show that, at 3 A cm^{-2}, ohmic losses, mainly caused by the membrane, contribute to about 85% or more of the overall differential resistance.

Ohmic losses at high current density decrease proportionally with the decrease of the membrane thickness thus allowing the achievement of much higher current densities at the same voltage efficiency. However, a significant reduction of the membrane thickness will also produce a proportional increase of the gas crossover especially under high differential pressure operation (pressurised hydrogen and non-pressurised oxygen) causing significant loss of faradaic efficiency beside the occurrence of safety issues and the impossibility to operate under low partial load. These are significant restrictions in term of system reliability and dynamic characteristics. After several decades of development, it seems that a further improvement of the proton conductivity of PFSA membranes is hard to achieve in the next years. Thus, the achievement of high current densities, as required to reduce the capital costs of PEM electrolysis systems, passes through a necessary reduction of the membrane thickness.

This strategy was already adopted in automotive PEM fuel cells. However, in the fuel cell automotive sector, the use of air blowers requires operation at very low pressure. Thus, for PEM fuel cells operating at ambient pressure, the use of membranes with a thickness of 10-20 µm does not represent an issue in terms of gas crossover and fuel utilisation. This is instead a relevant drawback when a differential pressure of about 20-30 bars is applied between the cathode and anode compartments in PEM electrolysers. In this case, the industry standard is a Nafion 117 membrane with a thickness of 170 µm, in dry form, offering proper protection against gas crossover.

A decrease of the membrane thickness from 170 to 50 µm would produce a significant decrease of the ohmic drop with a corresponding large increase of reaction rate at a similar voltage efficiency. However, the corresponding increase of hydrogen concentration in the oxygen stream caused by the thinner membrane needs to be minimised. In principle, a one percent loss of faradaic efficiency does not represent a significant drawback if the hydrogen production rate is increased significantly (e.g. twice or more) allowing for a corresponding decrease of the capital costs of the entire system. Instead, a one percent increase of the hydrogen concentration in the oxygen stream would be dramatic for the electrolyser safety characteristics and for the possibility to operate under partial load.

The conventional electrocatalysts used at the anode of a PEM electrolyser are mainly based on Ir metal, which is oxidised on the surface during operation, IrO_2 and IrRuOx. Unfortunately, these oxidised catalysts are not efficient for molecular hydrogen oxidation. Thus, permeated hydrogen is released into the outlet anodic stream. Generally, a PEM electrolyser is equipped with an external catalytic gas recombiner (e.g. a Pt/Al_2O_3 bed) to promote H_2/O_2 recombination in the gas phase, especially to reduce the oxygen contamination level in the produced hydrogen gas. However, these purification systems are allocated outside the PEM electrolysis stack for technical reasons. Their use allows essentially a purification of the produced gases but it does not allow improving the internal safety of the stack device.
Based on these considerations, the approach used in this work was to integrate a thin layer of a hydrogen oxidation catalyst in the membrane-electrode assembly, between the membrane and the IrRuOx anode catalyst layer, in order to decrease the concentration of hydrogen in the oxygen stream well below the safety limit. This concept was demonstrated in the presence of a thin (90 µm) PFSA membrane, in a wide range of operating current densities (from 0.3 to 3 A cm^{-2}) and differential pressures (up to 20 bar).
The approach of using a hydrogen oxidation catalyst at the anode can be also employed in combination to other strategies involving membrane modifications. As an example, the use of Pt nanoparticles inside the membrane, firstly used to promote internal humidification in fuel cells, can provide a useful internal recombination route for the permeated hydrogen and oxygen gases. However, this strategy requires a recast procedure for membrane production. Similarly, the casting method is also used when specific fillers are added into the membrane to increase the tortuosity factor for gas permeation. On the other hand, an excellent mechanical strength is required for the polymer electrolyte membrane in pressurised electrolysers applications. Thus, extruded membranes are usually employed. The present catalytic approach does not require any membrane modification if low gas permeation and proper faradaic efficiency are guaranteed by the polymeric electrolyte separator. Moreover, the approach here developed appears to be simpler than using a Pt electrode layer in between two membrane layers.
Thus, the oxidation catalyst here developed is integrated into the membrane-electrode assembly (MEA) to favour the oxidation to protons of the hydrogen permeated at the anode. The formed protons diffuse back to the cathode, under the electric field gradient effect, where these are reduced again to hydrogen. This causes a parasitic process that just produces a small decrease of faradaic efficiency; the overall loss of faradaic efficiency is less than 1% for reasonably thin PFSA membranes of about 90 µm thickness. However, as mentioned above, the limited loss of faradaic efficiency is largely compensated by a significant increase of the hydrogen production rate that is favoured by the use of thinner membranes.
Unfortunately, hydrogen oxidation catalysts based on bare Pt are easily oxidised on the surface to Pt-oxide during operation at the anode of an electrolysis cell. This causes a decrease of the oxidation activity. Such drawback also affects the Pt layer usually coated onto the Ti-foam current collector.
In this deliverable, the development of oxygen and hydrogen evolution electro-catalysts were carried out. The main approach for the anode catalyst were the improvement of the intrinsic activity and stability through tailoring anode catalyst surface chemistry, electronic effects and crystallographic orientation. The aim was to produce stable nanostructured solid solutions of Ir and Ru with a core-shell configuration consisting of Ir enrichment on the surface and optimised crystallographic orientation.
As for the anode catalyst, noble metal-based cathode catalysts was developed in order to provide corrosion resistance in acidic environment and appropriate catalytic activity for hydrogen evolution. The aim was to further reduce the cathode catalyst loading to less than 0.1-0.05 mg cm^{-2}, increase current density up to 4-8 A cm^{-2} while keeping the low overpotential characteristics of the hydrogen evolution process. Pt electrocatalysts for cathodic operation were supported on a stable carbon nanofibres support to substitute microporous carbon blacks.
A highly dispersed unsupported Pt-alloy, with low propensity to form Pt oxides, was used at the anode side of an electrolysis cell. This additional catalytic layer is confined between the perfluorosulfonic membrane and the IrRuOx anode catalyst. Electro-catalytic tests at high differential pressure were

restricted to the most promising Pt-based formulation down-selected from ex-situ catalytic tests. The catalyst screening process was carried out through gas-phase catalytic tests in a packed bed reactor allowing to rapidly identifying the properties for H_2-O_2 recombination back into water.
X-ray photoelectron spectroscopy (XPS) suggests the presence of a relatively lower Pt-oxide content on a PtCo alloy compared to bare Pt. From the ex-situ screening and XPS analysis of different Pt systems, we have selected the PtCo system for validating this approach in a single cell PEM electrolyser. The PtCo catalyst showed the capability to reduce significantly the hydrogen concentration in the oxygen stream at the anode in the presence of a PFSA membrane with reduced thickness. This approach allows for a large increase in reaction rate while avoiding safety issues.

2. ENHANCED CATALYSTS PREPARATION

2.1 ANODE ELECTROCATALYST

To achieve the aimed performance, efficiency and stability, anode catalysts based on Iridium are necessary to provide corrosion resistance in acidic environment and excellent catalytic activity for oxygen evolution that is the rate determining step of the electrolysis process. The main approach of this task regards the improvement of the intrinsic activity and stability through tailoring anode catalyst surface chemistry, electronic effects and crystallographic orientation. The aim is to produce stable nanostructured solid solutions of Ir and Ru with a core-shell configuration consisting of Ir enrichment on the surface and optimised crystallographic orientation.
Adams fusion method was used to prepare an $Ir_{0.7}Ru_{0.3}Ox$ electrocatalyst. Dry salts containing metal precursors ($IrCl_4 \cdot xH_2O$ and $RuCl_3 \cdot xH_2O$, Strem Chemicals) and $NaNO_3$ (Aldrich) were treated in a furnace at 500°C for 5 min. The fused salt-oxide product was cooled down, washed, filtered and dried in an oven at 80°C for all night. A pre-leaching procedure in $HClO_4$ (0.1 M, 80°C, 15 min) was used to completely remove the impurities providing a crystalline nanosized IrRu-oxide.

2.1.1 Physico-chemical properties of Anode catalyst

X-ray diffraction (XRD) was carried out using a Panalytical X-Pert instrument with a CuKa radiation. The diffraction patterns were interpreted using the Joint Committee on Powder Diffraction Standards (JCPDS). Scanning electron microscopy (SEM) was carried out with a FEI S-FEG XL30 microscope equipped with energy dispersive X-ray (EDX) spectrometer. The morphology and nanostructure was investigated by scanning transmission electron microscopy (STEM) carried out in a Cs corrected microscope CF-ARM Jeol operated at 200 kV, equipped with a SSD Jeol EDX spectrometer. The specimens were prepared by sample dispersion in alcohol and subsequently depositing a few drops of the suspension on a carbon-coated copper grid.
The X-ray pattern in Fig. 1 shows the typical reflections of the tetragonal rutile crystallographic structure of IrO_2 and RuO_2. However, the shift of the diffraction peaks towards higher Bragg angles (e.g. the 211 reflection occurs at 54.40° as shown in the inset of Fig. 1 with respect to 54.15° expected for IrO_2) indicates the occurrence of a lattice contraction as consequence of the formation of a solid solution. Moreover, the presence of a single diffraction peak at 66.5° in the region where two reflections, 310 and 112, of similar intensity typical occur in Ru or in separate IrO_2 - RuO_2 mixtures is also indicative of the presence of solid solution (Fig. 1).

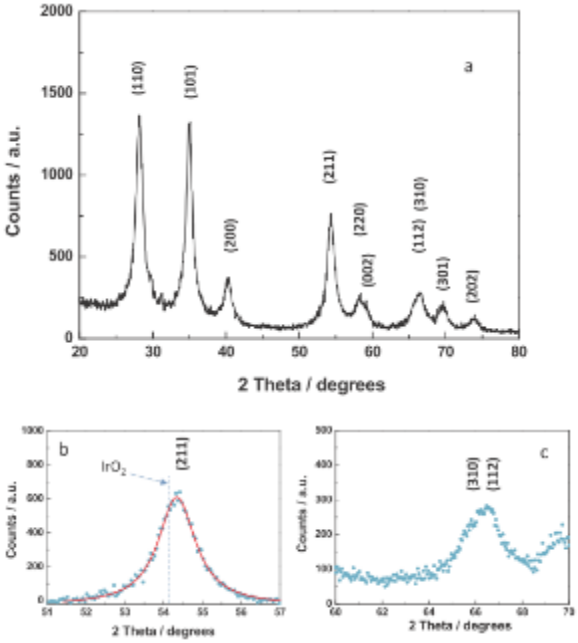

Fig. 1. A-c X-ray diffraction patterns of the anodic IrRuOx catalyst and high resolution scans of specific two theta regions.

A 70:30 at. composition for the solid solution IrO_2:RuO_2 is estimated from the shift of diffraction peaks in accordance with the nominal composition. This composition was selected to obtain complete solubilisation of RuO_2 in the IrO_2 lattice while avoiding excess of RuO_2 on the surface that may corrode in acidic environment through oxidation to RuO_4 and subsequent dissolution. The mean crystallite size determined from the Debye-Scherrer equation is about 7.6 nm. The IrRu-oxide catalyst morphology investigated by transmission electron microscopy, showed a mixture with small irregular shape particles and faceted particles (Fig. 2a and b).

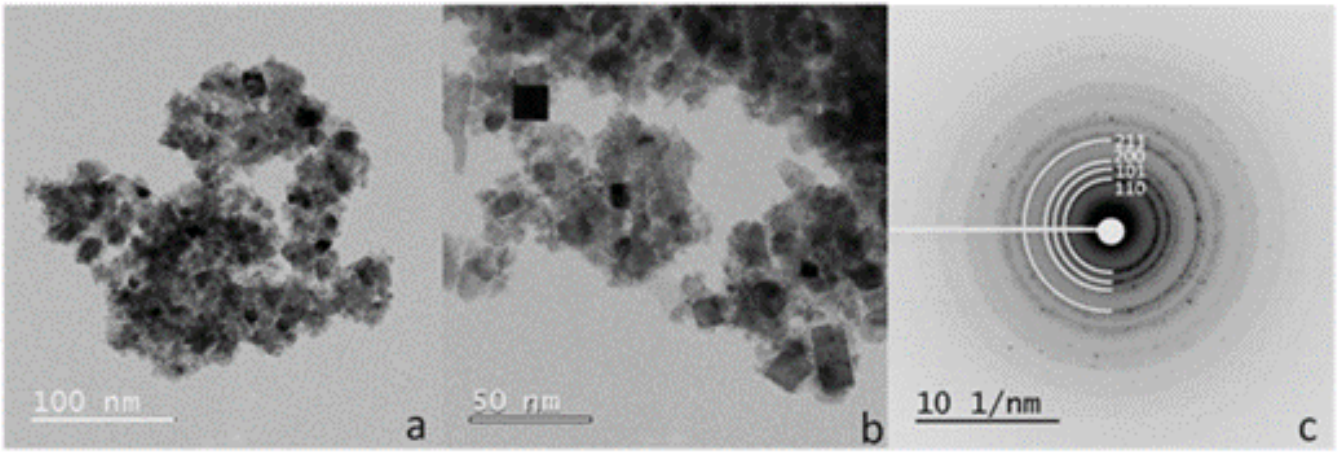

Fig. 2. A-c Transmission electron micrographs (a, c) of the anodic IrRuOx catalyst and electron diffraction pattern.

For what concerns the faceted particles, squared shape nanocrystals (2D-image) were clearly evident together with elongated or rod-like (rectangular shape) particles. Most of the square shape particles were characterized by a dimension smaller than 10–15 nm where a few rod-like particles showed a length up to 25 nm (Fig. 2b). Analysis at higher magnification (see below) showed the occurrence of very small

regular nanocrystals together with fine irregular particles (< 10 nm). A particle size distribution cannot be easily carried out for this type of morphology and particle shapes. However, it seems that the average crystal size estimated from the broadening of X-ray diffraction provides a good representation of the mean particle size of the material. Electron diffraction (Fig. 2c) essentially confirmed the rutile structure and the polycrystalline nature of this material whereas the broadening of the diffraction rings was indicative of the prevailing occurrence of very fine particles.
However, it should be pointed out that oxygen evolution is a structure sensitive reaction and the presence of small nanocrystals with well defined orientation (Fig. 3a), most of them show well defined (110) facets, as evident in the reciprocal space (Fig. 3a and b), may play a relevant role for the process.

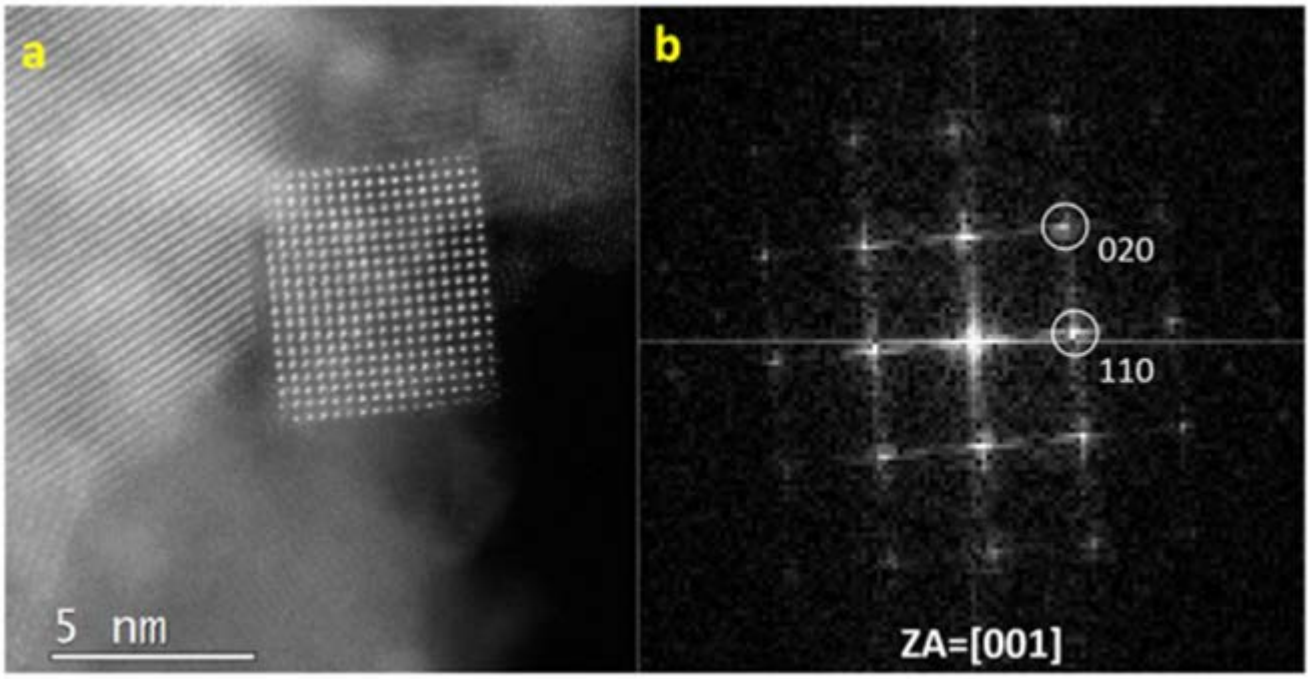

Fig. 3. A-b Microstructural properties of the IrRuOx anode catalyst.

Beside the microstructural aspects, the surface chemistry of this catalyst is very important in terms of both activity and performance. Scanning transmission electron microscopy (STEM) annular dark field imaging was also performed in parallel to Energy-dispersive X-ray spectroscopy (EDX) mapping (Fig. 4). In principle, the distribution of both Ir and Ru appears homogeneous along the agglomerate (Fig. 4).
However, it is noted that the contours (edges) of the agglomerate are more easily reproduced by the Ir M mapping (Fig. 4c) than the Ru mapping (Fig. 4d) as compared to the STEM BF and ADF images. The contours of the agglomerate observed from O K mapping (Fig. 4e) appear more similar to the Ir map even if the Ir M distribution better represents the agglomerate shape. According to this evidence, the surface contours of the agglomerate are mainly composed by Ir atoms whereas it is not exclude that some internal regions are enriched of Ru as it may be seen from the overlay image (Fig. 4f).
In particular, the shape of a large rectangular particle is well reproduced in terms of contours by the Ir mapping whereas the edges of this particle are less clear in both the Ru and O mapping (Fig. 4d and e). Interestingly, the Ir mapping (Fig. 4c) shows that the core of the rectangular shape particle is somewhat empty of Ir atoms and the same core regions are enriched with Ru atoms. The overlay image (Fig. 4f) confirms such aspect. This is a clear evidence of an enrichment of the core of faceted particles with Ru atoms whereas their surface is essentially composed of Ir atoms. The fact, that also oxygen atoms are less occurring on the surface would indicate the presence of sub-stoichiometric Ir atoms in the outermost layer.

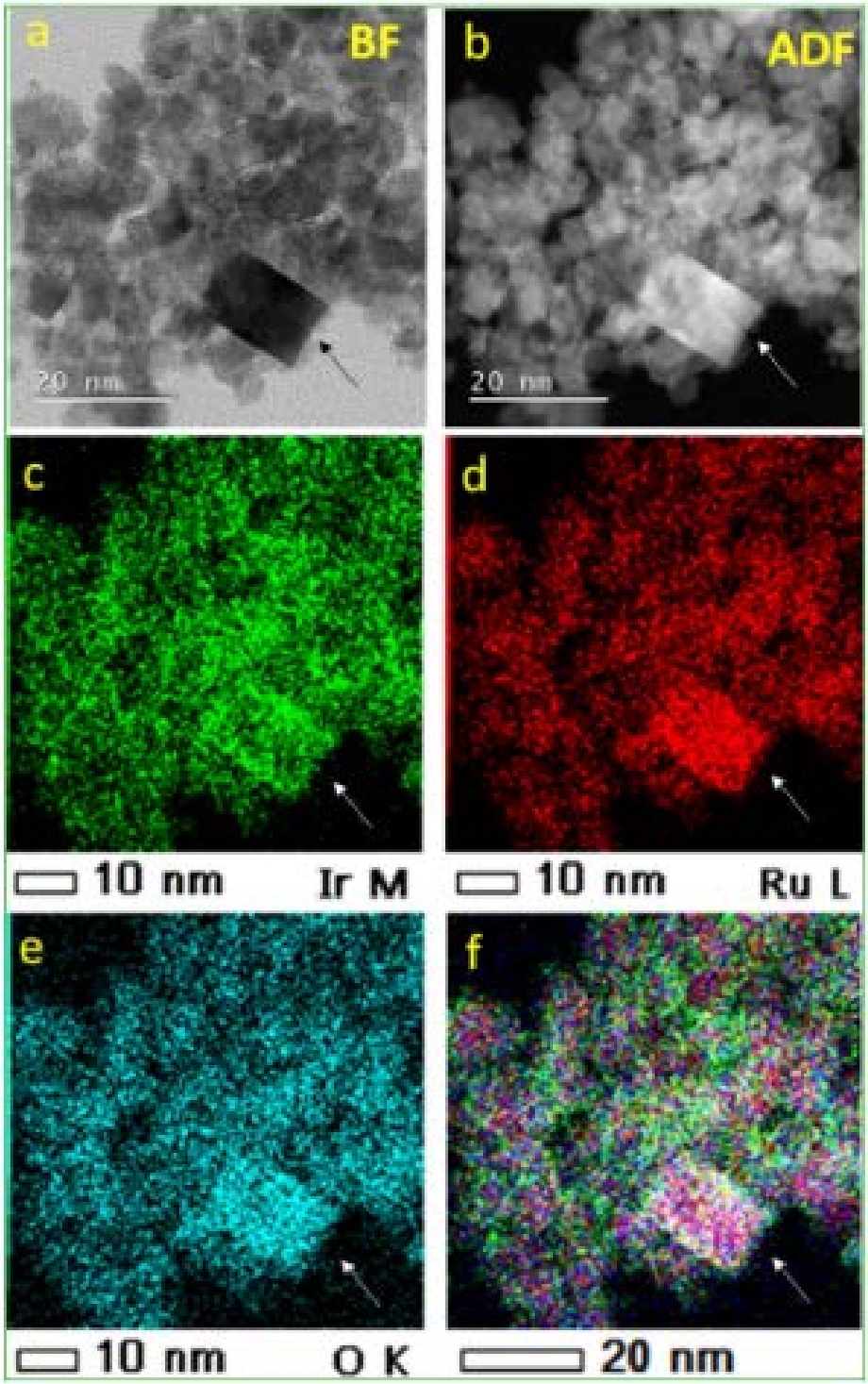

Fig. 4. a-f Bright field (a), annular dark field (b) imaging and EDX mapping (c-f) of the IrRuOx catalyst agglomerate at high magnification.

The total available surface area of an catalyst is usually determined by Brunauer–Emmett–Teller (BET) measurement using nitrogen adsorption/desorption at the liquid nitrogen temperature. Fig. 5 shows the BET analysis of IrRuOx. The BET surface area of this catalyst result 149 m^2/g with meso porous particle.

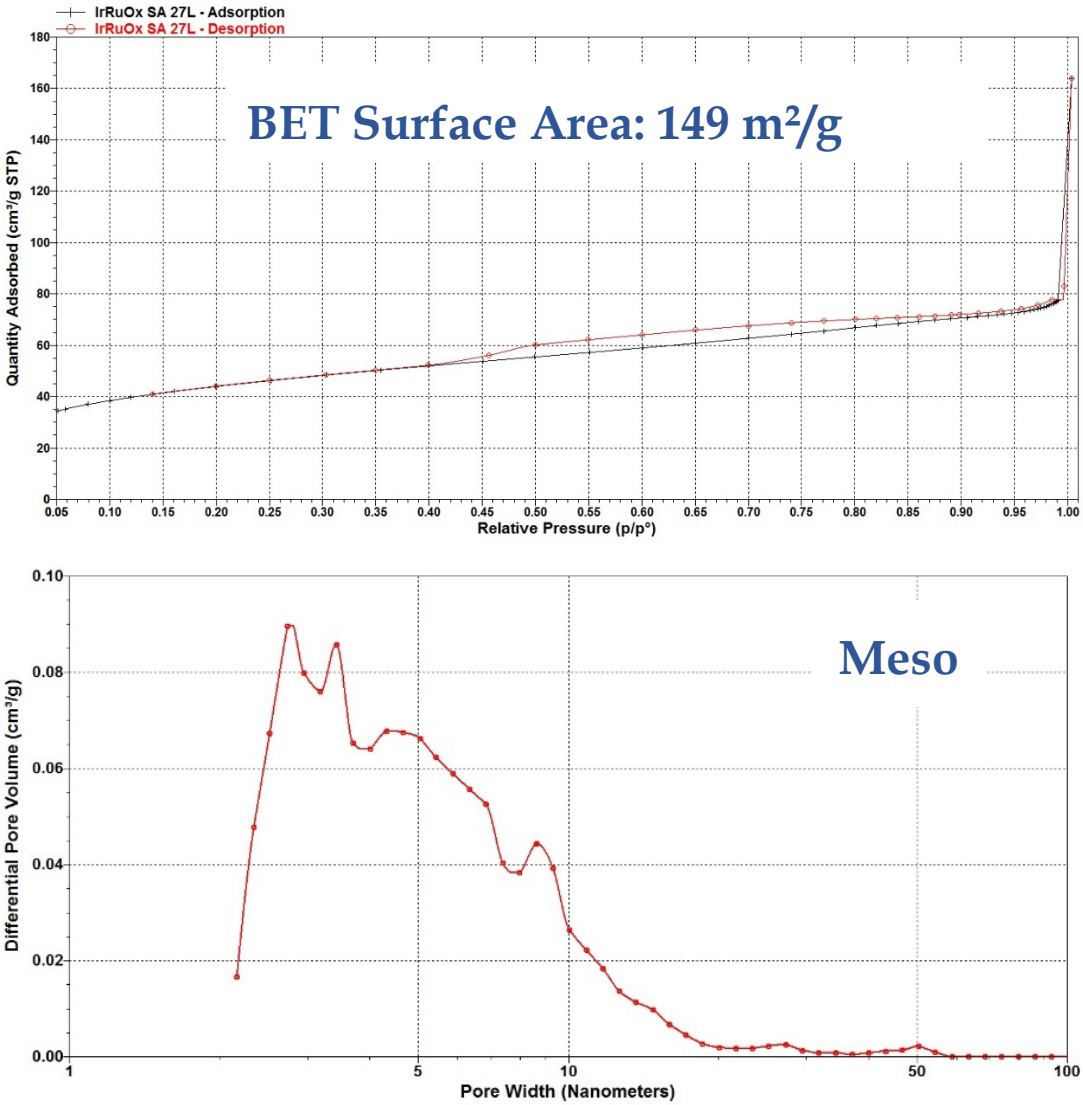

Fig. 5. BET analysis of IrRuOx.

2.2 CATHODE ELECTROCATALYST

As for the anode catalyst, noble metal-based cathode catalysts are necessary to provide corrosion resistance in acidic environment and appropriate catalytic activity for hydrogen evolution. These are essentially based on Pt or Pd. The aim of this task is to reduce the cathode catalyst loading (Pd or Pt) to less than 0.1-0.05 mg cm^{-2}, increase current density up to 4-8 A cm^{-2} while keeping the low overpotential characteristics of the hydrogen evolution process. This will require good anchoring of the noble metal phase (Pt or Pd) on the support with high dispersion of nanosized metal particles and no relevant mass transport limitations.

Three different preparation routes are selected as versatile process to obtain a noble metal-based cathode catalysts.

2.2.1 Sulphite complex route

The procedure consisted of the following steps: (1) a sulfite complex of Pt in an appropriate amount was decomposed by hydrogen peroxide to form an aqueous colloidal solution of Pt-oxide; (2) then, these particles were adsorbed onto carbon black to form PtOx/carbon; and (3) finally, the amorphous oxides on carbon were reduced in a hydrogen stream to form the supported Pt metal particles. The resulting powders were characterized by X-ray diffraction (XRD) to determine the crystallographic structure and by transmission electron microscopy (TEM) to evaluate the morphology. Figure 6 shows Pt cubic and Carbon support hexagonal crystallographic structures with 3.3 nm of Pt crystalline size. In the inset, the TEM imagine evidence the good Pt dispersion on carbon.

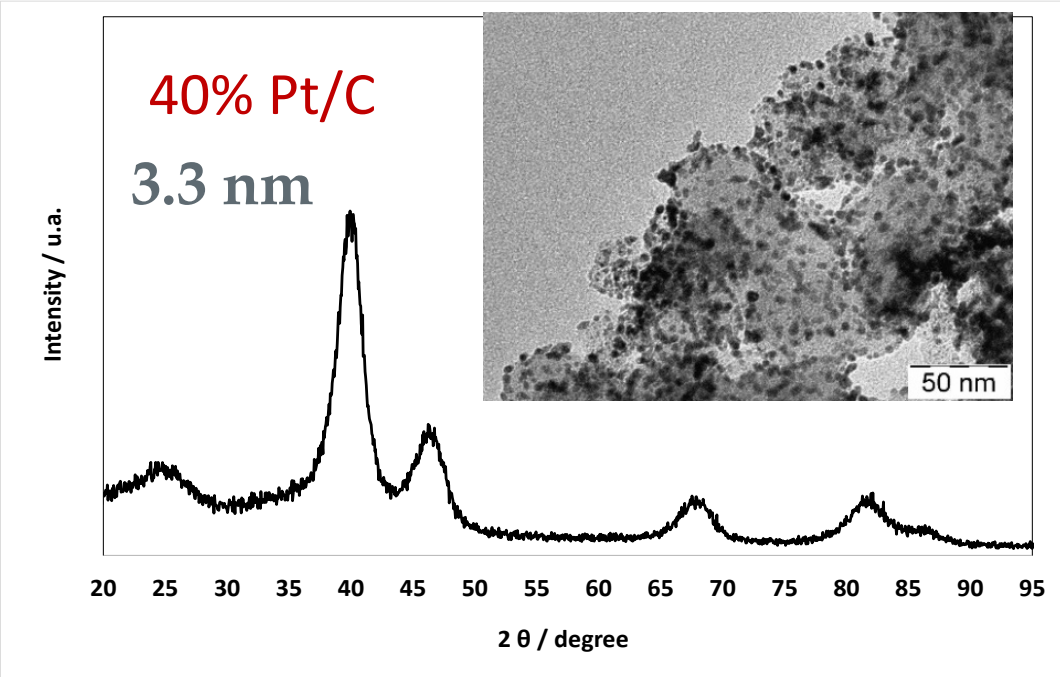

Fig. 6. XRD and TEM analysis of 40% Pt/C prepared by sulfite complex route

2.2.2 Catalytic decomposition method

Carbon nanofibers were prepared by catalytic decomposition of methane in a fixed-bed reactor (650°C - 700°C). Platinum supported on carbon nanofibers was synthesized by a water in oil microemulsion route. Briefly, it consists on the preparation of a microemulsion composed by composed by 16.5% surfactant (polyethylene glycol dodecyl ether, Brij®30, Sigma–Aldrich), 3.9% aqueous solution containing the platinum precursor (0.05 M H_2PtCl_6) and 79.6% n-heptane as the hydrophobic phase. Subsequently, the appropriate amount of support is dispersed in the microemulsion under sonication to achieve a metal concentration in the catalyst of 20 wt.%. The reduction step involves the slow addition of sodium borohydride in excess and finally the catalyst is thoroughly washed with ethanol and water to remove the chemicals used during the synthesis, and dried overnight at 60°C.

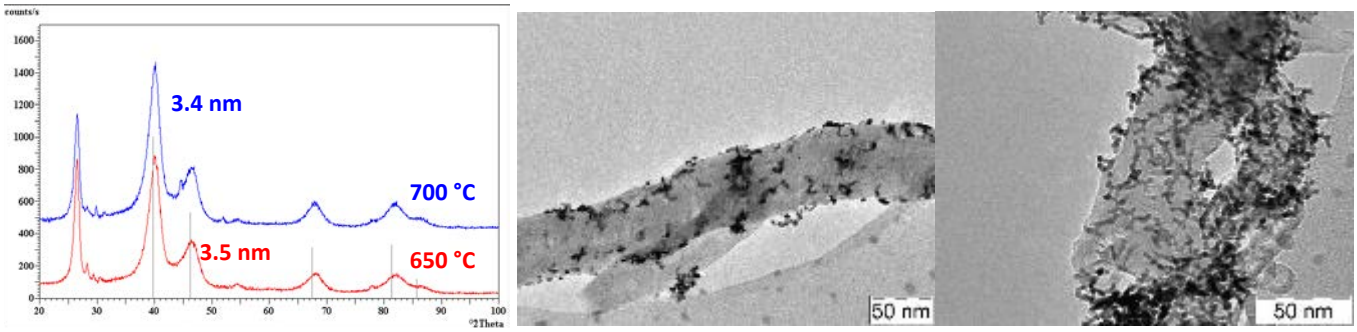

Fig. 7. XRD and TEM analysis of 20% Pt/C prepared by catalytic decomposition method

2.2.3 Electrospinning

The Pt/CNF sample was synthesized by electrospinning method starting from Platinum(II) acetylacetonate $Pt(AcAc)_2$ (Sigma Aldrich, 97%) and polyacrylonitrile (PAN) (Sigma Aldrich, Mw = 150,000) used as precursors of metal and carbon nanofibers, respectively. An amount of 0.16 g of $Pt(AcAc)_2$ was mixed with a solution containing 0.12 g of PAN in 2 g of N,N Dimethylformamide (DMF) (Sigma Aldrich, 99.8%). The mixture was kept under magnetic stirring at 60°C for 1 hour. The obtained solution was loaded into a 20 ml glass syringe provided with a 21G stainless steel needle. A voltage of 17 kV was applied to the solution jet while a flow rate of 0.77 mL h^{-1} was maintained by using a syringe pump. An electrospun layer consisting on $Pt(AcAc)_2$ /PAN was deposited on the graphite target placed at a distance of 12 cm from the needle tip. The temperature and the relative humidity were kept constant at 21°C and less than 40% respectively thanks to an environmental heating system. The electrospun layer was subjected to a first stabilization treatment at 270°C in air for 30 min and subsequently to a carbonization treatment at 900°C for 1 h under a helium (He) flow of 80 ml/min with a heating rate of 5°C/min. In fig. 8 is reported the physico-chemical characterization of electrospun Pt/CNF sample. It is possible to observe from SEM and XRD analyses (fig. 8a and 8c) the formation of well-defined carbon nanofibers with a high degree of graphitization. The TGA analysis (fig. 8b) revealed the presence of a low amount (13%) of platinum within the sample probably due to a platinum loss during the thermal treatments at 270°C and 900°C. TEM analysis, reported in figure 8d, also confirmed the presence of a small amount of platinum nanoparticles distributed along the carbon nanofibers.

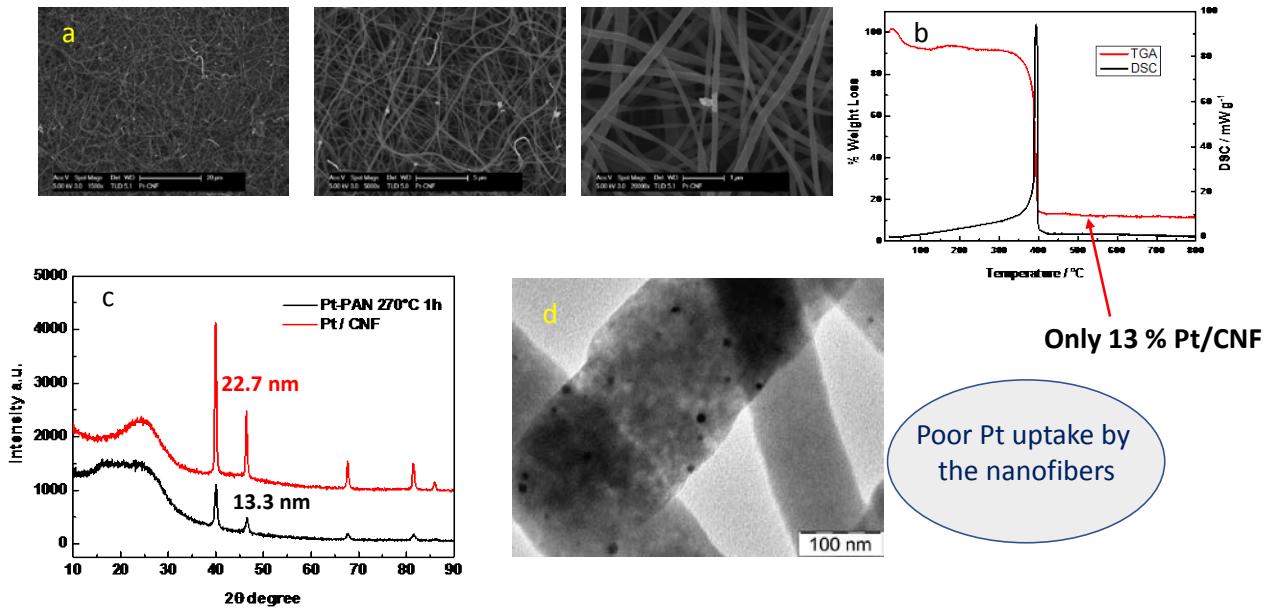

Fig. 8. Physico-chemical characterizations of electrospun Pt/CNF; a) SEM images at different magnification, b) TGA/DSC curves, c) XRD diffraction patterns, d) TEM analysis

A synthesis optimization of electrospun Pt/CNF was carried out in order to increase the platinum content within the sample. A first thin layer of PAN was deposited on the graphitic target by the electrospinning of 1 ml of a 10% PAN solution in DMF. Then, the solution containing 0.16 g of $Pt(AcAc)_2$ and 0.12 g of PAN in 2 g of DMF was electrospun on the first layer. Finally, a third layer of PAN was deposited as well as the first layer in order to block and avoid the removal of Platinum during the successive thermal treatments at 270°C in air and 900°C in He. The electrospinning procedure was kept the same as the first preparation method. SEM and XRD analysis (fig. 9a and 9c) showed the formation of well-defined carbon nanofibers with a high graphitization degree and a good distribution of the Pt nanoparticles on the CNF. Moreover, an increase in the Pt percentage on CNF from 13% to 30% was revealed by TGA analysis.

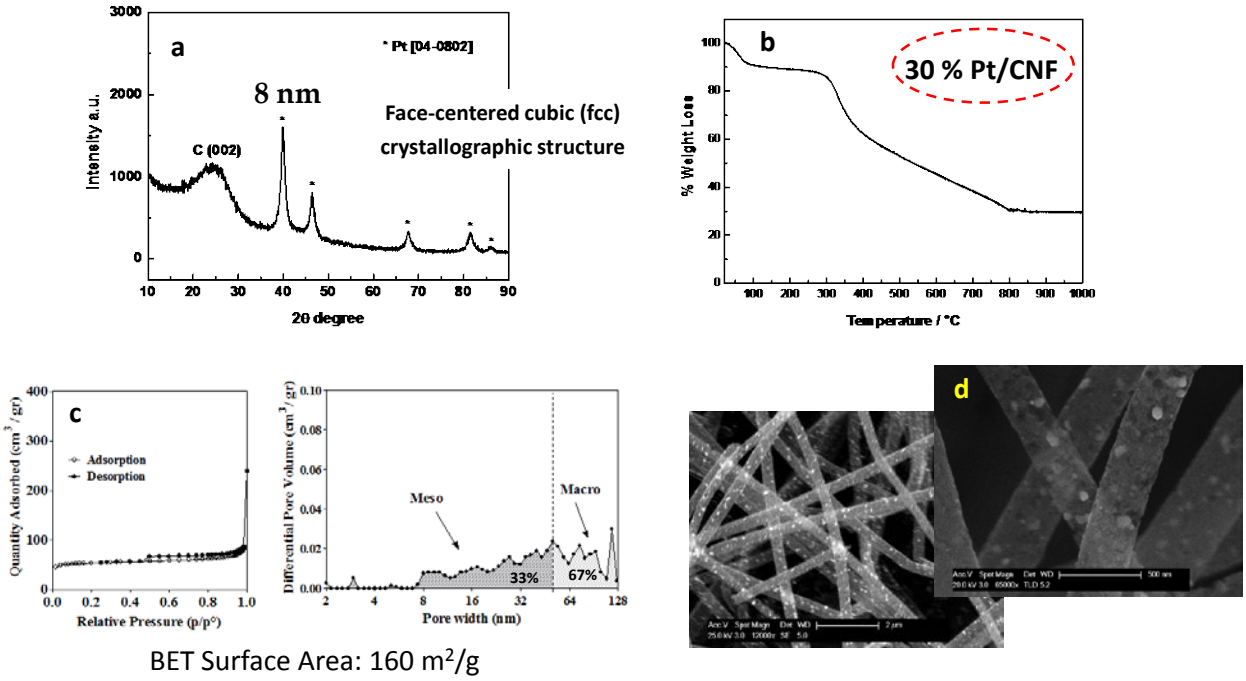

BET Surface Area: 160 m^2/g

Fig. 9. Physico-chemical characterizations of electrospun Pt/CNF: a) XRD diffraction patterns; b) TGA curve; c) BET analysis; d) SEM images at different magnification.

3. CATALYTIC ACTIVITY, ELECTROCHEMICAL PERFORMANCE AND STABILITY OF ENHANCED CATALYSTS

Membrane-electrode assemblies were prepared by using different Aquivion® membranes.
The commercially available extruded short-side chain Solvay Aquivion® membrane (E98-09S) with an equivalent weight (EW) of 980 g eq^{-1} and a thickness of 90 µm was prepared by melt extrusion of polymer resin in $–SO_2F$ form. Membrane thus obtained was treated with $NaOH/H_2O$ solution and then with HNO_3/H_2O transforming $–SO_2F$ in $–SO_3H$ group.

The recast short-side chain Solvay Aquivion® membrane (C98-09S) with an equivalent weight of 980 g eq^{-1} and a thickness of 90 µm was prepared starting from commercial water-based Aquivion® D98-25BS dispersion (EW: 980 g/mol, 25 wt% solid content). An advanced version (C98-09S Adv 1) for this dispersion was formulated till obtaining the following composition: Aquivion® polymer (22 wt%), deionized water (36 wt%), n-propanol (32 wt%) and N-methylpyrrolidinone (10 wt%). The dispersion thus obtained was cast on tempered glass using a doctor blade (Zehntner ZUA2000) and an automatic applicator (Zehntner ZAA2300). After deposition, the film underwent a three-steps heating cycle in a vent oven: 1 h at 65°C, 1 h at 90°C and 1 h at 190°C. Membrane was then peeled off from glass using demineralized water. It was dried in a vent oven at 80°C.
The ionomer dispersion (D98-06AS) used for electrode manufacturing in the MEAs had similar structure/composition of the membrane. The cathode catalyst (40% Pt/C), prepared by sulphite complex route, was spread on membrane. A carbon cloth (GDL ELAT from ETEK) was used as backing layer. The Pt loading was of 0.1 mg cm^{-2}. The ionomer Aquivion content in the cathode layer was 28 wt.% after drying. For the oxygen electrode, a slurry composed of 85 wt.% catalyst and 15 wt.% (dry weight) ionomer Aquivion® was prepared. The slurry was directly deposited onto one face of the membrane by using a spray coating technique. The anode metal catalyst loading was 0.34 mg cm^{-2}. A Ti fibre mesh was used as backing layer for the anode side (Scheme 1).

Cathode

Formulation:	Pt/C
Loading:	~ 0.1 mg/cm^2
Deposition method:	Spray at 80°C on membrane
Composition:	62% (Pt/C) + 28 wt. % D98 06AS
Backing layer	carbon cloth based GDL (HT ELAT)

Aquivion Membrane

Anode

Formulation:	IrRuOx
Metal Loading:	~ 0.34 mg/cm^2
Deposition method:	Spray at 80 °C on membrane
Composition:	85 wt. % IrRuOx + 15 wt.% D98 06AS
Backing layer	Ti fibre mesh

Scheme 1. MEAs composition

MEAs were thus subjected to a hot-pressing procedure and subsequently installed in an electrolysis test fixture. The PEM single cell (5 cm^2) electrolyser performance was evaluated in a temperature range from 30° to 90°C under atmospheric pressure. Deionised water was circulated by a pump at a flow rate of 2 ml min^{-1} and supplied to the anode compartment. The water was maintained at the same temperature of

the cell. Measurements of electrochemical impedance spectroscopy (EIS, 1 MHz -10 mHz) were carried out by an Autolab PGSTAT 302 Potentiostat/Galvanostat equipped with a 20 A booster (Metrohm). The series resistance was determined from the high frequency intercept on the real axis of the Nyquist plot. The polarization resistance was taken as the difference between the extrapolated low frequency intercept and the high frequency intercept on the real axis.

Polarization curves (I-V) were carried out in the galvanostatic mode by recording the cell voltage vs. the imposed current density. The current density values are selected according to a logarithm variation. This is determined by the specific form of the Volmer-Butler equation, which indicates an exponential increase of current as function of the overpotential. Thus, there is the need to sample a large number of data at low current and less at high current; whereas, the trend at high currents is essentially governed by the ohmic drop and thus the linear relationship of the Ohm law. Mass transport effects with the corresponding inflection point in the polarisation curves at high current densities are less frequent in PEM electrolysis polarisation.

3.1 MEAs Characterization

Polarisation curves and electrochemical impedance spectroscopy of PEM electrolysis MEAs based on extruded and recast Aquivion® membranes have been carried in a wide range of temperature (from 30 to 90°C) and atmospheric pressure with a reduced overall precious catalyst loading (0.44 mg cm^{-2} MEA).

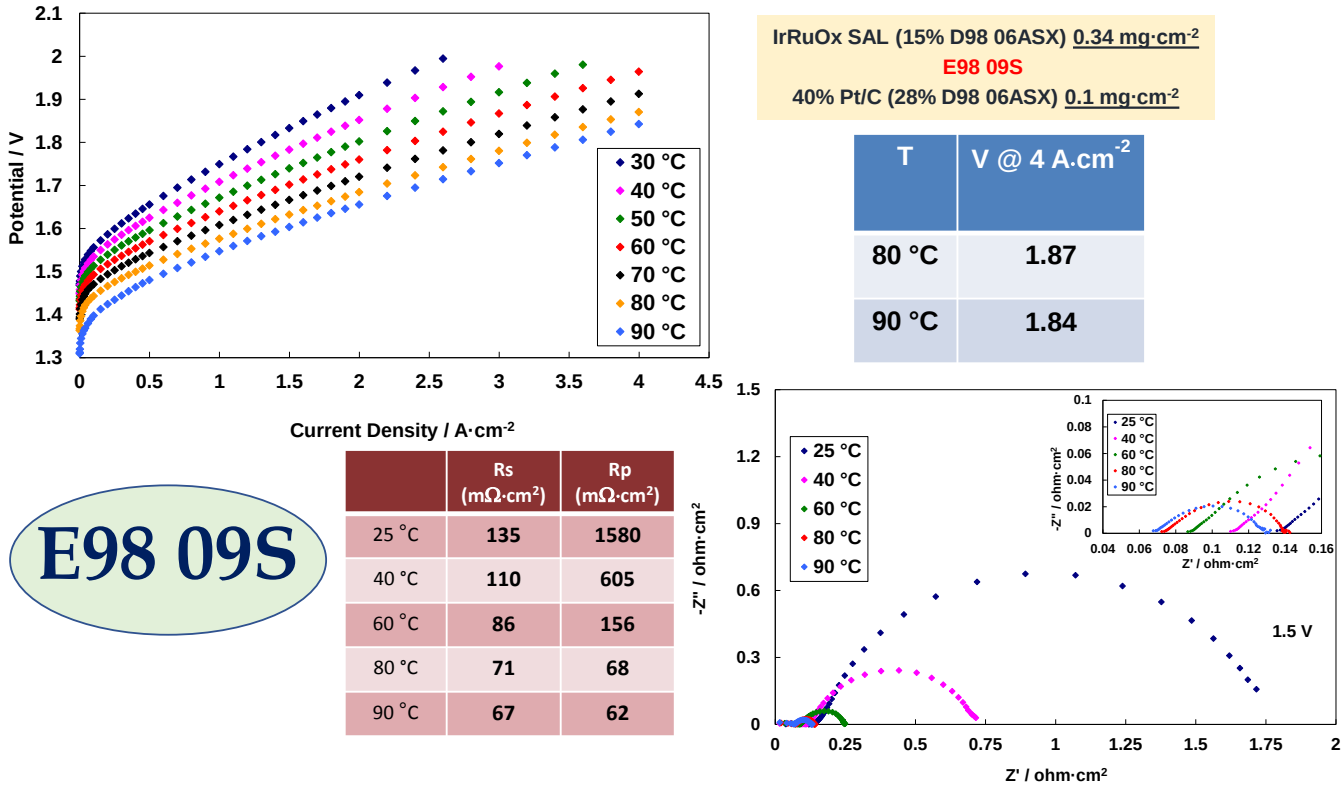

Fig. 10. Polarization curves and ac-impedance spectra at 1.5 V at different temperatures for the MEA with extruded membrane.

The polarisation curves for the electrolysis cell based on the extruded (E98-09S) membrane (Fig. 10) show a relevant increase of current density (hydrogen production rate) with temperature at a fixed cell voltage (voltage efficiency). This clearly evidences the benefits of operating the electrolyser at high temperature

in increasing the cell efficiency. At 90°C, a current density of 4 A cm^{-2} is obtained at 1.84 V with an overall noble metal catalyst loading (Ir+Ru+Pt) of 0.44 mg cm^{-2} and a membrane thickness of 90 µm.
Electrochemical impedance analysis was carried out under a constant voltage efficiency condition (Fig. 10). This provides insights into the effects related to the variation of the reaction rate with the temperature. The possibility of achieving high reaction rates at fixed cell voltages is inversely related to series resistance (high frequency intercept on the real axis of the Nyquist plot) and polarisation resistance (difference between low and high frequency intercepts). The ac-impedance spectra in the low voltage region (1.5 V) show that both series and polarization resistances decreased as the temperature increased. The lowest Rs and Rp values were recorded at 90°C i.e. 67 mΩ·cm^2 and 62 mΩ·cm^2, respectively.

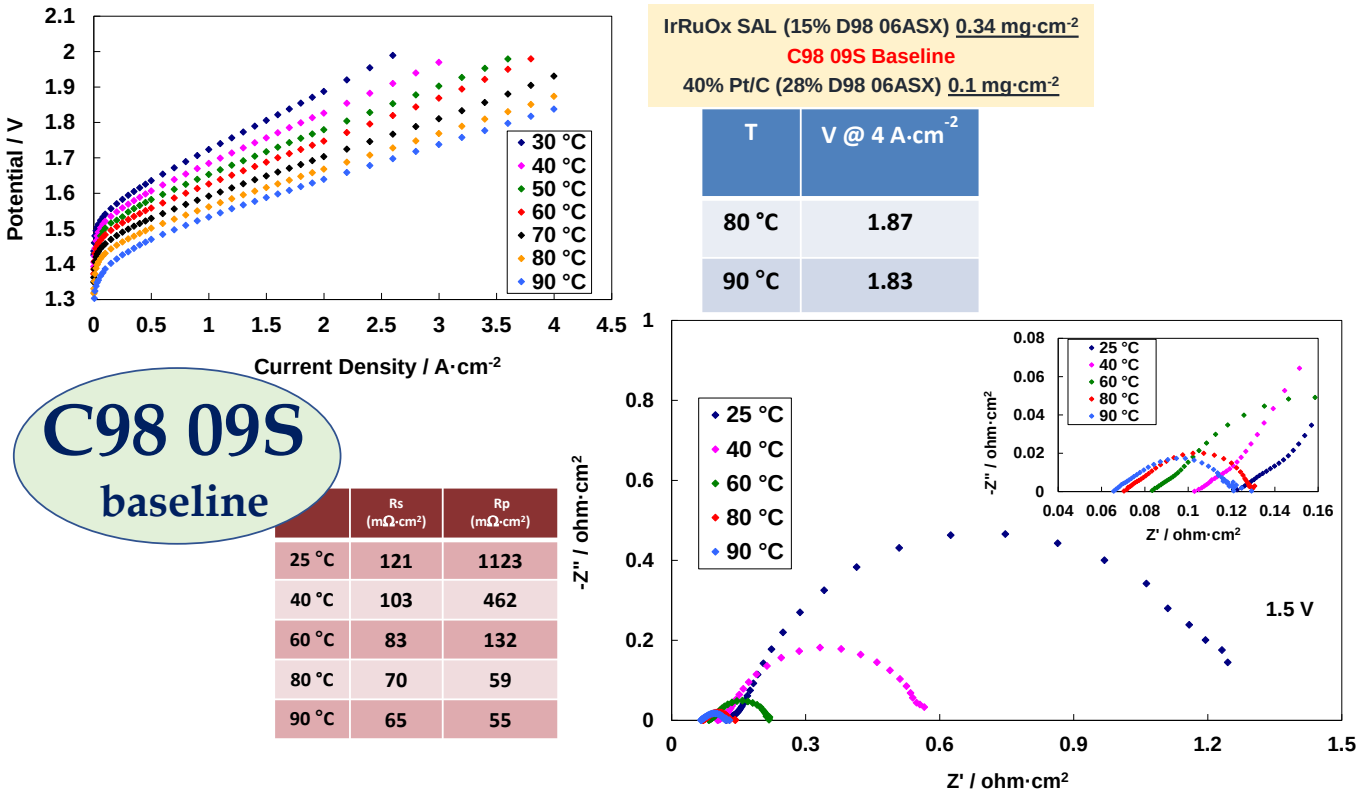

Fig. 11. Polarization curves and ac-impedance spectra at 1.5 V at different temperatures for the MEA with baseline recast membrane.

The Baseline recast membrane (C98-09S bas) based MEA shows polarisation characteristics similar to the extruded membrane-based MEA (Fig. 11). However, the EIS spectra at 1.5 V shows, at low temperature, a relevant difference, i.e., the overall impedance is about 1.2 Ohm cm^2 for the recast membrane versus 1.7 Ohm cm^2 for the extruded polymer-based MEA under the same conditions. This essentially derives from a larger polarisation resistance in the case of the extruded membrane (1.58 vs. 1.12 Ohm cm^2). Having used the same electrodes, catalyst and ionomer loadings in both MEAs, this difference is ascribed to the different interfacial properties arising from the different membrane characteristics.

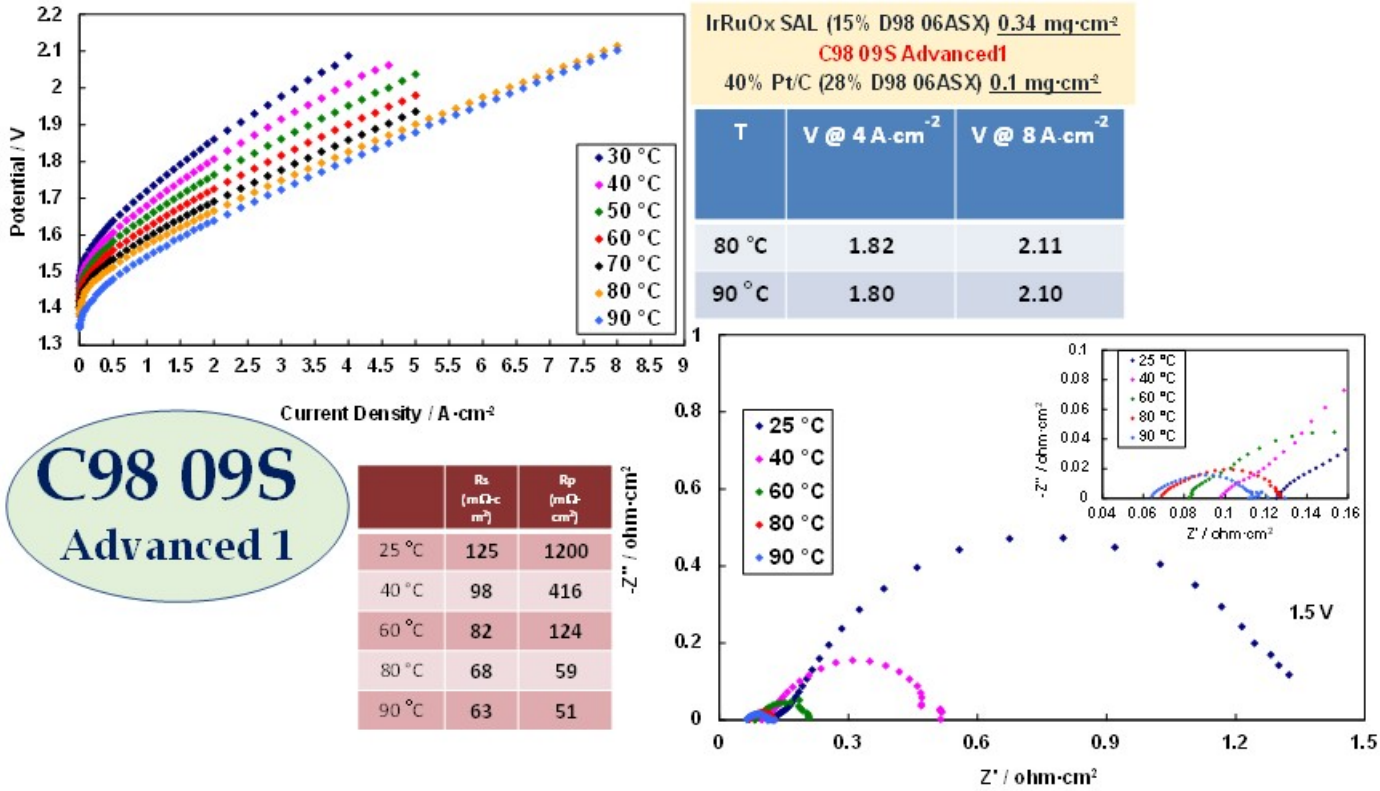

Fig. 12. Polarization curves and ac-impedance spectra at 1.5 V at different temperatures for the MEA with advanced recast membrane.

A further increase of performance was observed in polarization and impedance spectroscopy for the Advanced recast membrane (C98-09S Ad) based MEA (Fig. 12).

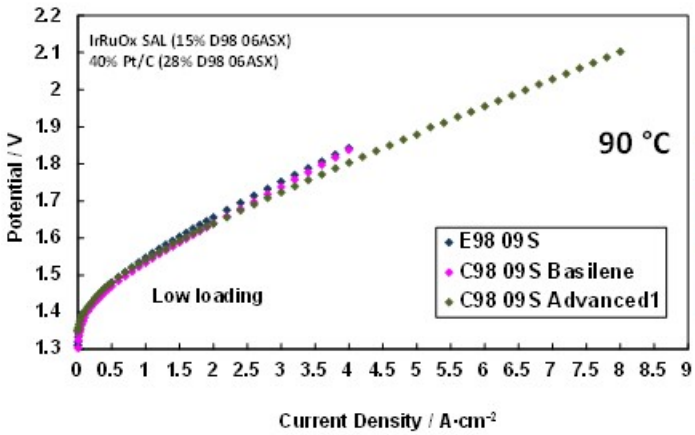

	Potential / V	Current density / A cm-2	Potential / V	Current density / A cm-2
E98 09S	1.84	4	-	-
C98 09S Baseline	1.83	4	-	-
C98 09S Advanced1	1.80	4	2.10	8

	Rs (mΩ·cm²)	Rp (mΩ·cm²)
E98 09S	67	62
C98 09S Baseline	65	55
C98 09S Advanced1	63	51

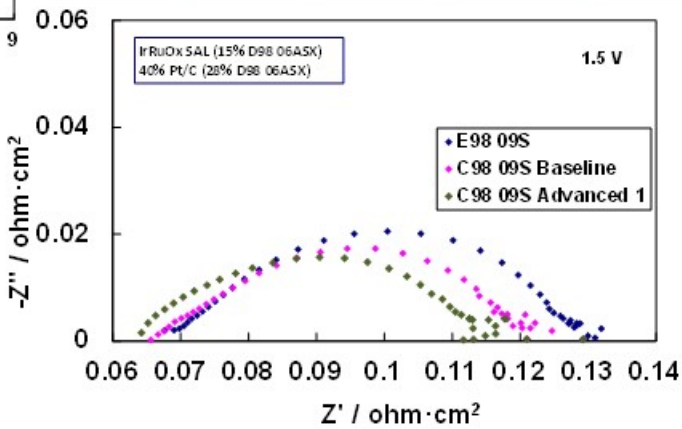

Fig. 13. Comparison of Polarization curves and ac-impedance spectra at 1.5 V and 90°C for the MEAs with Extruded and Recast membranes

A comparison of the polarisation curves and ac-impedance spectroscopy at 90°C for the three MEAs (Fig. 13) shows a small but evident performance in the case of the recast Advanced membrane resulting from a lower potential at high current density. The series resistance is just slightly lower for the recast Advanced membrane according to the fact that both membranes are based on the ionomer and have the same thickness. This is due to the catalyst-electrolyte interface, performance improves with a decrease of the membrane surface roughness dimension.

Another formulation of MEA was characterized in a single cell with a decrease of the amount of ionomer and with a lower thickness of membrane (scheme 2). Previous investigation have indicated that this may be a possible route to decrease the recoverable losses. The same metal catalysts loading was used for this MEA i.e. 0.44 mg/cm^2.

Cathode

Formulation:	Pt/C
Loading:	~ 0.1 mg/cm^2
Deposition method:	Spray at 80°C on membrane
Composition:	67% (Pt/C) + 23 wt. % D98 06ASX
Backing layer	carbon cloth based GDL (HT ELAT)

Aquivion Membrane: E98-05S

Anode

Formulation:	IrRuOx
Metal Loading:	~ 0.34 mg/cm^2
Deposition method:	Spray at 80 °C on membrane
Composition:	90 wt. % IrRuOx + 10 wt.% D98 06ASX
Backing layer	Ti fibre mesh

Scheme 2. MEA composition

IrRuOx SAL (*10% D98 06ASX*) 0.34 mg·cm^{-2}
E98 05S
40% Pt/C (*23% D98 06ASX*) 0.1 mg·cm^{-2}

T	V @ 4 A·cm^{-2}	V @ 8 A·cm^{-2}
70 °C	1.87	2.18
80 °C	1.83	2.15
90 °C	1.80	2.12

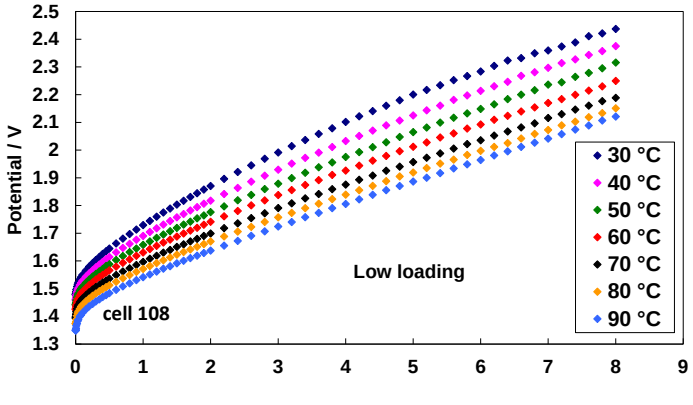

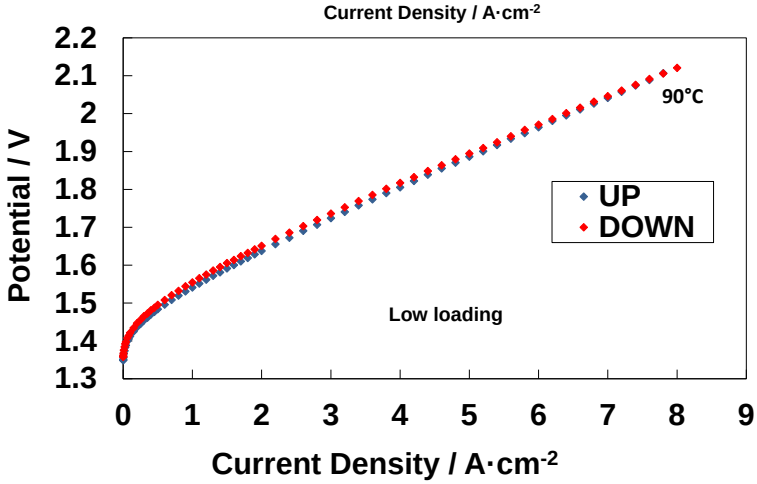

Fig. 14. Polarization curves at different temperatures for the MEA with extruded (E98-05S) membrane.

Fig. 14 shows single cell polarization curves for the IrOx-based MEA in the range of temperature from 30°C to 90°C under atmospheric pressure. Also for this cell, there is a progressive increase of performance with temperature. The best performance at high current densities for water electrolysis was obtained at 90°C. The potential values at 4 and 8 A·cm^{-2} and 90°C were 1.8 V and 2.12 V, respectively. Similar performance was observed for the polarization measurement in both cases if starting at high or low current.

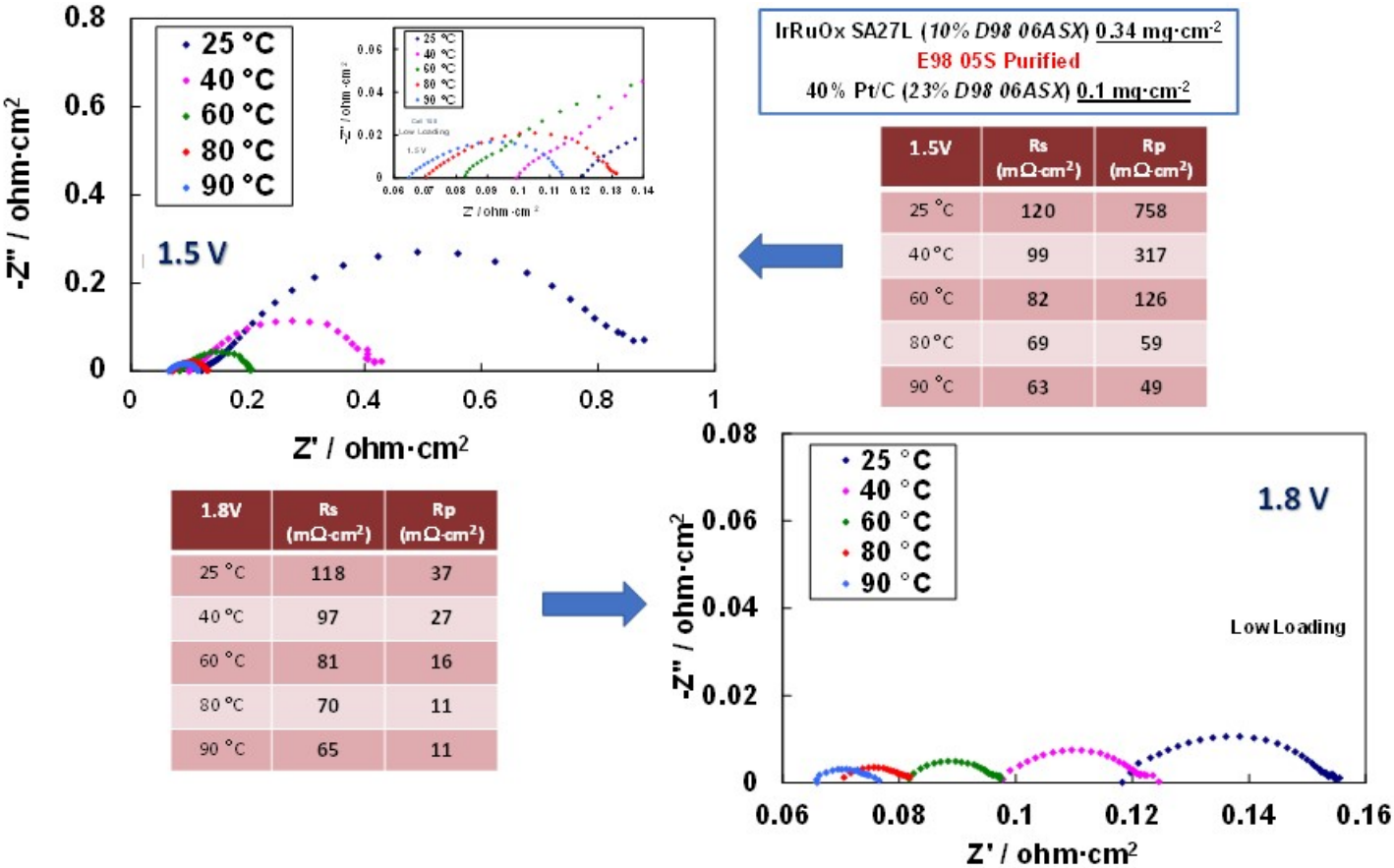

1.5V	Rs (mΩ·cm²)	Rp (mΩ·cm²)
25 °C	120	758
40 °C	99	317
60 °C	82	126
80 °C	69	59
90 °C	63	49

1.8V	Rs (mΩ·cm²)	Rp (mΩ·cm²)
25 °C	118	37
40 °C	97	27
60 °C	81	16
80 °C	70	11
90 °C	65	11

Fig. 15. Ac-impedance spectra at 1.5 V and 1.8 V at different temperatures for the MEA with extruded (E98 05S) membrane.

The impedance plots (Nyquist) obtained by the EIS analysis at 1.5 and 1.8 V for the E98 05S membrane-based cell are reported in Fig. 15. Also in this case, both Rs and Rp decreased as a function of the increase of the temperature. A 90°C and 1.5 V the values were 63 mΩ·cm^2 and 49 mΩ·cm^2 for the Rs and Rp, respectively. Whereas at 90°C and 1.8 V the values were 65 mΩ·cm^2 and 11 mΩ·cm^2 for the Rs and Rp, respectively.

As recommended procedure, it is considered appropriate to carry out a membrane purification treatment in 1 M H_2SO_4 even if the benefits are no yet clear since series resistance is similar to untreated samples.

One of the major concerns in reducing the catalyst loading is stability. In this regard, steady-state durability studies have been performed to provide the relevant information. The MEAs prepared for this study have been evaluated for their durability in steady state tests of 2000 h at 1, 3 and 4 A·cm^{-2} and 80°C (Figure 16). As can be seen, in these tests the cell voltage increases rapidly in the first 100 hours due to MEA conditioning and mass recoverable losses due to the mass transport constraints; thereafter, there is a slow linear variation of potential with time due to MEA degradation.

The performance decay rate for the developed catalysts in the presence of the Aquivion® membrane E98-05S is corresponding to 4.4 µV/h when the last 1000 h are considered in the overall 2000 h durability test. This trend represents the overall catalyst and membrane degradation because the first 1000 h are essentially affected by reversible losses. The catalysts show also good stability when operated with C98-09S membrane. These results are promising and in line with MS7 milestone; however, it is clarified that

these results have been achieved at the single cell level (not in the stack as required by MS7) and at 80 °C instead of 90 °C as indicated in the DoW. However, these results indicate that the developed catalysts can be appropriate for the large area MEAs to be tested in the stack configuration.

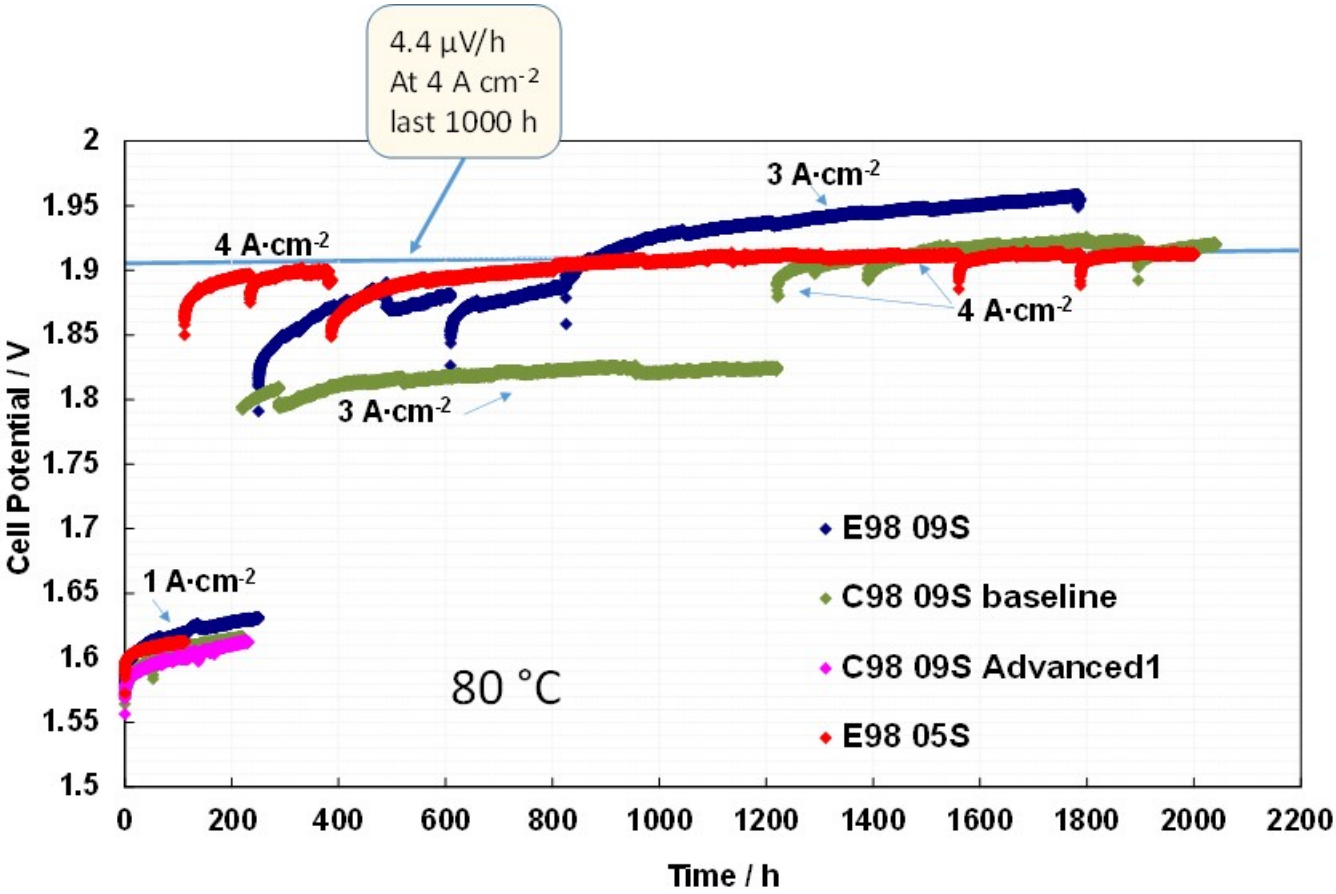

Fig. 16. Comparison of catalysts durability tests at 80°C and 1, 3 and 4 A·cm^{-2} for the different MEAs tested with Extruded and Recast membranes

4. ANODE INTEGRATED RECOMBINATION CATALYST

Various Pt-based materials (unsupported Pt, PtRu, PtCo) were investigated as catalysts for recombining hydrogen and oxygen back into water. The recombination performance correlated well with the surface Pt metallic state. Alloying cobalt to platinum was observed to produce an electron transfer favouring the occurrence of a large fraction of the Pt metallic state on the catalyst surface. Unsupported PtCo showed both excellent recombination performance and dynamic behaviour. In a packed bed catalytic reactor, when hydrogen was fed at 4% vol. in the oxygen stream (flammability limit), 99.5% of the total H_2 content was immediately converted to water in the presence of PtCo thus avoiding safety issues. The PtCo catalyst was thus integrated in the anode of the membrane-electrode assembly of a polymer electrolyte membrane electrolysis cell. This catalyst showed good capability to reduce the concentration of hydrogen in the oxygen stream under differential pressure operation (1-20 bar), in the presence of a thin (90 µm) Aquivion® membrane. The modified system showed lower hydrogen concentration in the oxygen flow than electrolysis cells based on state-of-the-art thick polymer electrolyte membranes and allowed to

expand the minimum current density load down to 0.15 A cm^{-2}. This was mainly due to the electrochemical oxidation of permeated H_2 to protons that were transported back to the cathode. The electrolysis cell equipped with a dual layer PtCo/IrRuOx oxidation catalyst achieved a high operating current density (3 A cm^{-2}) as requested to decrease the system capital costs, under high efficiency conditions (about 77% efficiency at 55°C and 20 bar). Moreover, the electrolysis system showed reduced probability to reach the flammability limit under both high differential pressure (20 bar) and partial load operation (5%), as needed to properly address grid-balancing service.

4.1 Experimental

The Pt-based hydrogen oxidation catalysts here investigated were two Pt alloys, i.e. PtRu (60:40 at.) and PtCo (75:25 at.), and Pt black. These recombination catalysts were synthesised by the sulphite complex procedure to form amorphous oxides. These were successively reduced in diluted hydrogen (10 % vol. H_2 in argon at 300°C) to form unsupported catalysts. Compared to conventional supported Pt catalysts, carbon support was avoided. At the anode of an electrolysis process, the high operating potential window causes rapid oxidation of carbon to CO_2. The catalysts were pre-leached in 0.1 M perchloric acid at 80°C in order to remove both impurities and unalloyed atoms from the surface.

The Pt-based catalysts were first assessed in terms of H_2 oxidation/recombination capability in the presence of oxygen in a packed bed catalytic reactor operating at 80°C and atmospheric pressure. Isothermal profiles of reagents and products were acquired by using a quadrupole mass spectrometer as an analytical tool (ThermoStar) equipped with a heated (150°C) fast-response inlet capillary system. In each cycle, the catalyst was preliminarily treated under O_2 atmosphere, after which a mixture H_2/O_2, with a nominal hydrogen percent in the oxygen stream of 4 vol.% (simulating extreme operating conditions for the cell), was admitted into the reactor, maintaining stationary conditions until the stabilization of signals was reached. Thereafter, the catalyst was again exposed to an oxygen atmosphere before starting a new cycle.

In a specific experiment, the PtCo (75:25 at.) catalyst was completely wetted inside the packed–bed reactor under a flow of nitrogen carrier saturated with distilled water through a bubbler kept at 60°C by a thermostatic bath (Julabo F12-ED, USA). This allowed getting a water vapor pressure of 0.196 atm at a weight hourly space velocity (WGSV) of 1 gH_2O/gcat/h. Before feeding the dry 4% vol. H_2-O_2 stream, the catalyst was exposed to a flow of pure (dry) oxygen. The next cycles were carried out with dry gases. Before each new cycle, the catalyst was exposed again to a flow of pure oxygen.

The down-selected PtCo catalyst was assessed in situ for the conversion of permeated hydrogen. A pressurised cell set-up was used in combination with a micro gas chromatograph (Varian Micro GC). The scheme of the electrolysis plant in shown in Fig. 17.

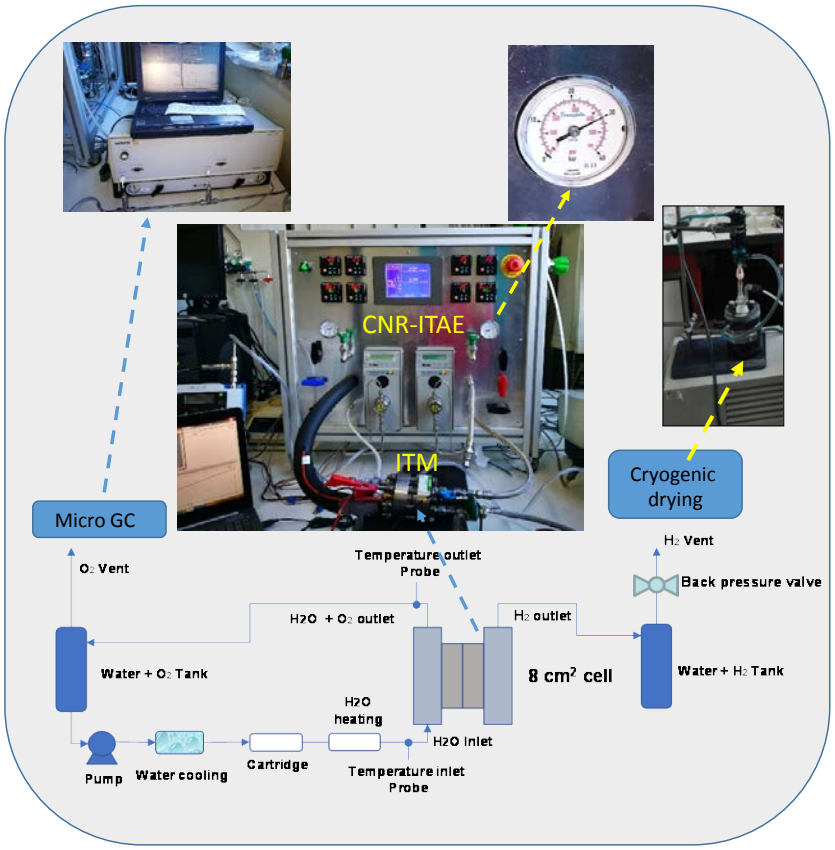

Fig. 17. Scheme and pictures of the CNR-ITAE high differential pressure electrolysis plant equipped with high pressure ITM Power (UK) cell and a micro gas-cromatograph for the determination of the hydrogen concentration in the outlet stream at the anode

For the single cell characterisation, a short-side chain Solvay Aquivion® (Fig. 18) membrane (E98-09S) was used in combination with IrRuOx (70:30 at.) at the anode and 30% Pt/C (Ketjenblack® carbon) at the cathode of the PEM electrolyser (Fig. 19).

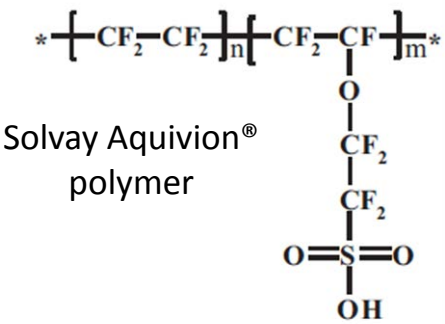

Fig. 18. Solvay Aquivion® chemical formula.

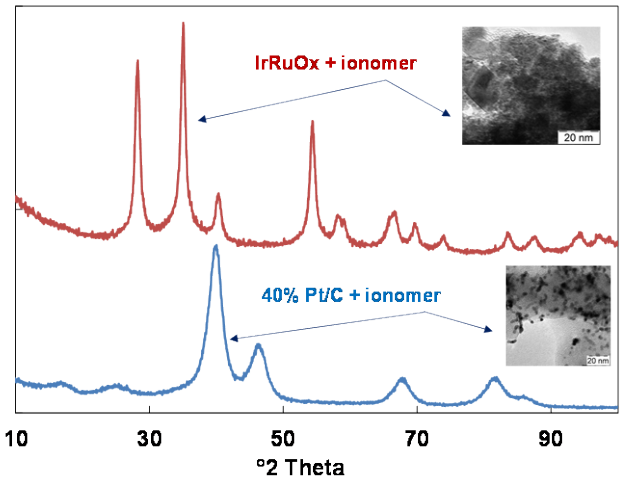

Fig. 19. X-ray diffraction and transmission electron microscopy of the IrRuOx and Pt/C-based catalytic inks used at the anode and cathode, respectively

Catalysts and membrane properties are described in previous papers. The membrane-electrode assembly preparation was carried out according to a catalyst-coated membrane (CCM) approach by spraying the catalyst ionomer inks onto the membrane. CCMs were hot-pressed at 190°C to favour hot bonding of the catalytic layers to the membrane at a temperature higher than the glass transition temperature of the Aquivion® polymer. In the bare MEA, the catalyst - ionomer ink consisted of 25% wt. Aquivion® ionomer (D98-06AS) and 75 % wt. Pt/C catalyst at the cathode, and 15% wt. Aquivion® ionomer and 85 % wt. IrRuOx catalyst at the anode.

The PEM electrolysis cell was operated up to a current density of 3 A cm^{-2} in the presence of low Pt (0.2 mg Pt cm^{-2}) and IrRuOx (0.3 mg Ir+Ru cm^{-2}) loadings at the cathode and anode, respectively. The approach of both minimising the precious metal loadings with respect to the state-of-the art (2-3 mg cm^{-2} Ir at the anode and 0.5 mg cm^{-2} Pt at the cathode) and increasing the operating current density is one of the preferred routes to decrease the capital costs of the PEM electrolysis system.

In the MEA modified with the hydrogen oxidation catalyst, the specific unsupported Pt-Co alloy was coated onto the membrane and the IrRuOx layer was coated on the top to form a dual layer anode. A spraying technique was used and the Aquivion® ionomer content in both composite anode inks was kept at 15% wt. The Pt loading in the oxidation layer at the anode was 0.1 mg cm^{-2}, the other catalyst loadings were the same of the bare MEA.

Titanium diffusion layers/current collectors (Bekaert Toko Metal Fiber Co.) were used at both anode and cathode in contact with the CCM. No Pt coating was used for these diffusion layers to avoid interfering with the PtCo catalyst for the hydrogen oxidation at the anode.

An ITM POWER (UK) pressurised electrolysis single cell test fixture was used in combination with an in-house (CNR-ITAE) developed test station (Fig. 17). The active area (geometrical electrode area) of the MEA was 8 cm^2. A power supply (TDK GEN 25-400-MD-3P400) was used to carry out polarisation experiments. An Autolab Metrohm potentiostat /galvanostat equipped with a 20 A current booster and FRA (frequency response analyser) was used to perform electrochemical impedance spectroscopy (EIS). Polarization curves were performed in the galvanostatic mode by recording the cell voltage vs. the imposed current density. A stepwise increase of current was used. Electrochemical impedance analysis was performed in he potentiostatic mode at 1.5 V and 1.8 V. The frequency was varied from 100 kHz to 100 mHz in the single sine mode with a sinusoidal excitation signal of 10 mV pk-pk. In all experiments, milli-Q Integral, Millipore deionized water was heated at 55°C before being supplied to the cell anode with a flow rate of 1 $mL \cdot min^{-1}$ cm^{-2}. The inlet water temperature was assumed as the cell temperature.

Physicochemical properties of the materials were examined by scanning electron microscopy – energy dispersive X-ray analysis (SEM-EDX) using a FEI FEG–XL30 instrument, transmission electron microscopy (TEM) was carried out with a FEI CM12 microscope and X-ray diffraction (XRD) was made by using a Panalytical X-Pert diffractometer equipped with a CuKa as radiation source. X-ray photoelectron spectroscopy was carried out with a PHI 5800-01 spectrometer. Spectra were obtained using a monochromatic Al Ka X-ray source and acquired with a pass energy of 187.85 eV for survey and 11.75 eV for high resolution spectra, respectively. BET surface area of the catalysts was measured with Thermo Fisher Scientific sorptomatic instrument.

4.2 Result and discussion

4.2.1 Structural and chemical characterisation of the Pt-based recombination catalysts

With regard to the hydrogen oxidation catalysts investigated in this study, PtRu was selected to obtain a bifunctional effect for H_2 oxidation at the Pt sites and water oxidation on the surface of RuOx species which are formed under anodic conditions. PtCo was instead chosen because cobalt in the alloy can transfer electrons to platinum atoms thus keeping Pt in a reduced state. A PtCo alloy with 3:1 atomic ratio was selected since this was characterised by a proper electronic effect while avoiding an excess of Co atoms on the surface that could affect the Pt activity in electrocatalytic processes. For the PtRu catalyst, in order to promote water oxidation in combination with hydrogen oxidation/recombination, the optimal atomic ratio for the bifunctional mechanism should be about 1:1, as in the case of the methanol electro-oxidation process (dehydrogenation of methanol on Pt in combination with water displacement on contiguous Ru sites). However, to provide a comparison between PtCo and PtRu catalysts with similar atomic ratio, also a PtRu 75:25 sample was investigated. The atomic ratio for both bimetallic samples was studied by energy dispersive X-ray analysis (EDAX) after a pre-leaching in perchloric acid (Figs. 20 and 21). The final atomic ratio was 75:25 for PtCo, 60:40 and 75:25 for PtRu samples. EDAX spectra showed larger oxygen content in PtRu 60:40 compared to the other catalysts (Figs. 20 and 21).

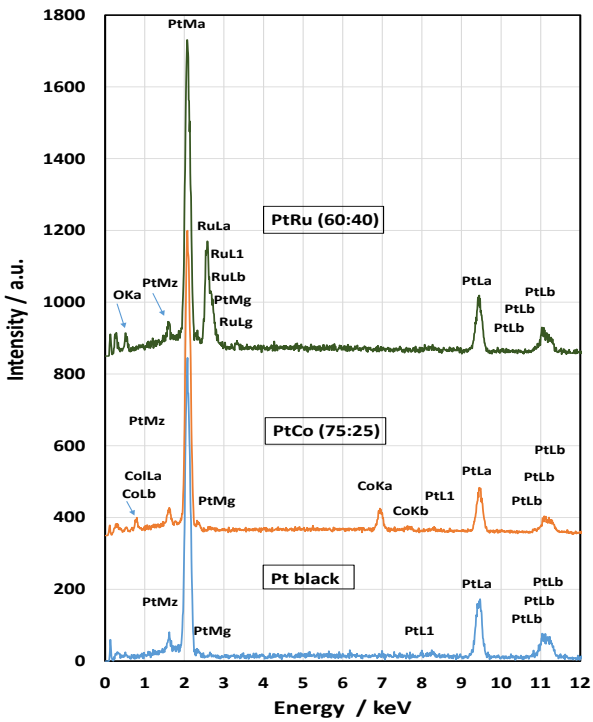

Fig. 20. Energy dispersive X-ray analysis of the recombination/hydrogen electro-oxidation catalysts.

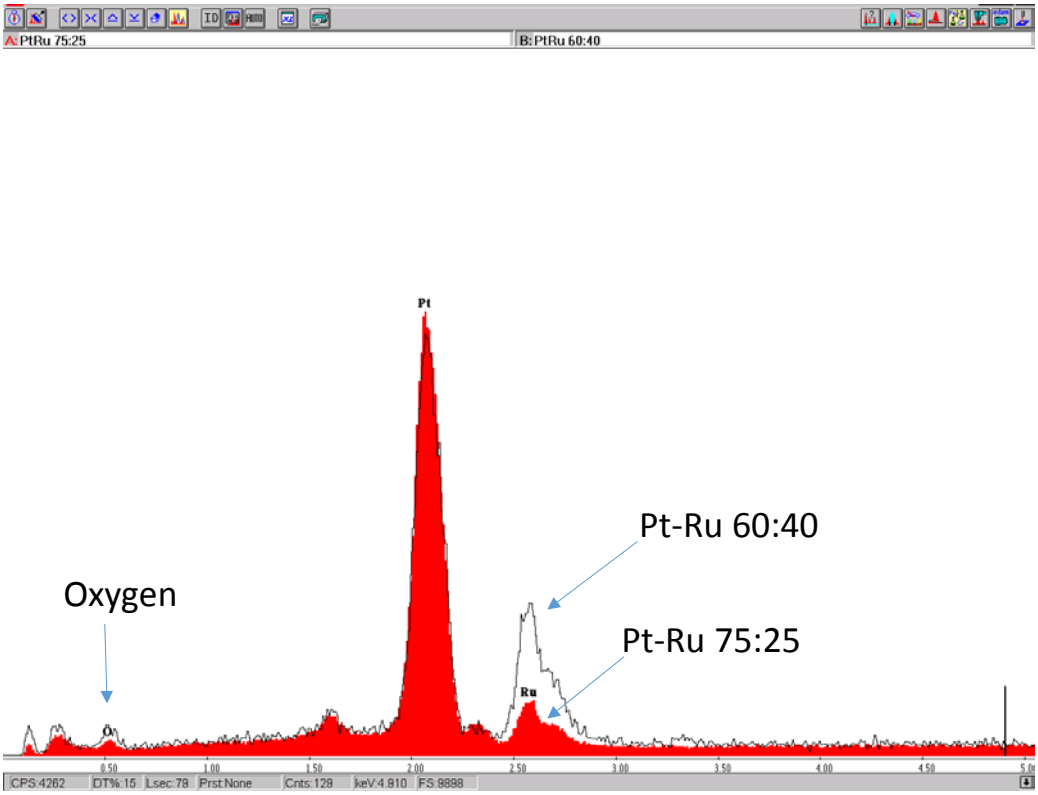

Fig. 21. Comparison of energy dispersive X-ray analysis spectra of the PtRu 60:40 and PtRu 75:25 catalysts.

Structural and morphological analyses (Fig. 22-25) showed a good dispersion and a face-centered cubic phase for both Pt alloys. The peak shift towards higher Bragg angles compared to Pt black (Fig. 22b) indicates in both cases the occurrence of an alloy. The observed shift is in accordance with the atomic contents in the bimetallic systems. From the broadening of the diffraction peaks (Fig. 22a-b and 23), a crystallite size of 6.4, 2.7, 3.6 and 6.9 nm was determined for Pt black, PtRu 60:40, PtRu 75:25 and PtCo, respectively, by using the Debye-Scherrer law.

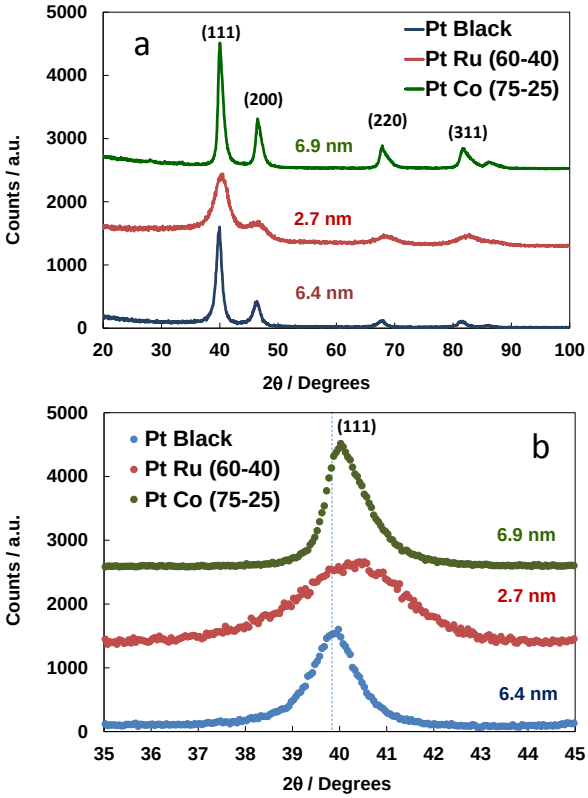

Fig. 22. X-ray diffraction patterns of the recombination/hydrogen electro-oxidation catalysts; a) full range; b) magnification of the Pt (111) reflection region.

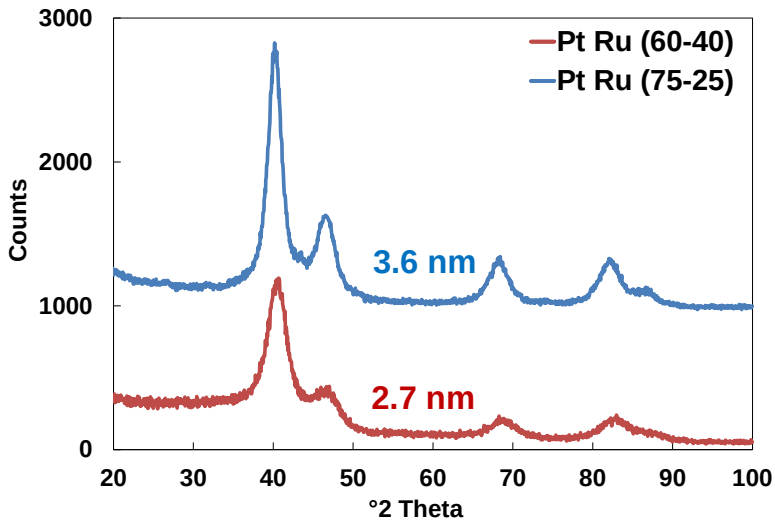

Fig. 23. X-ray diffraction patterns of the catalysts based on Pt Ru 60:40 and Pt Ru 75:25.

SEM analysis (Fig. 24-25) showed a sponge-like structure characterised by fine particles for all these unsupported catalysts. TEM analysis showed the presence of properly dispersed catalyst agglomerates which were composed of finer particles in the case of the PtRu unsupported catalyst compared to PtCo (Fig. 24). The Pt particle size in Pt black was in between that of PtRu and PtCo. Due to the relevant agglomeration, which is very common for the unsupported catalysts, it is not easy to estimate precisely the particle size distribution. However, it is clear that the presence of Ru mitigates the growth of the Pt particles during the thermal reduction in hydrogen determining a finer structure (Fig. 24) with a crystallite

size from XRD much lower than that of Pt black and PtCo (Fig. 22). This is also evident from TEM analysis at higher magnification (Fig. 26).

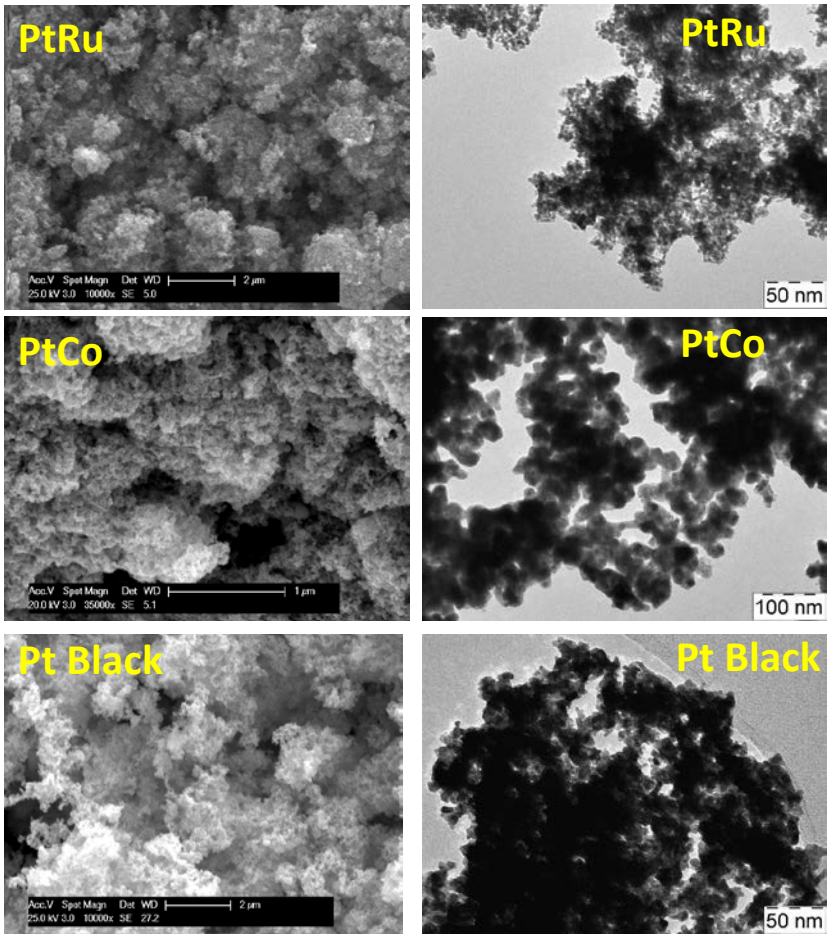

Fig. 24. Scanning (left) and transmission (right) electron micrographs of the recombination / hydrogen electro-oxidation catalysts.

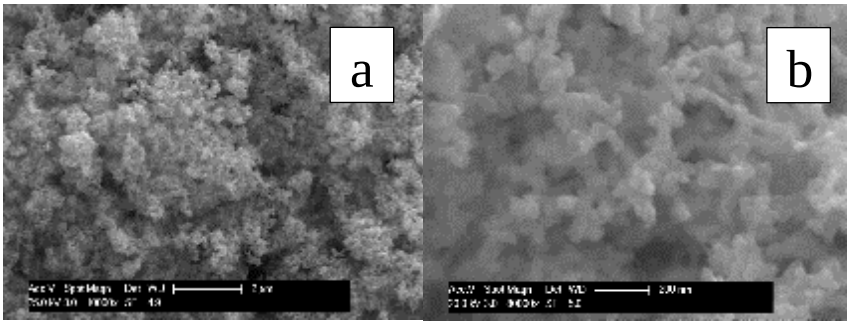

Fig. 25. SEM micrographs of the Pt Ru 75:25 catalyst at different magnifications; (a) 10 kx and (b) 80 kx.

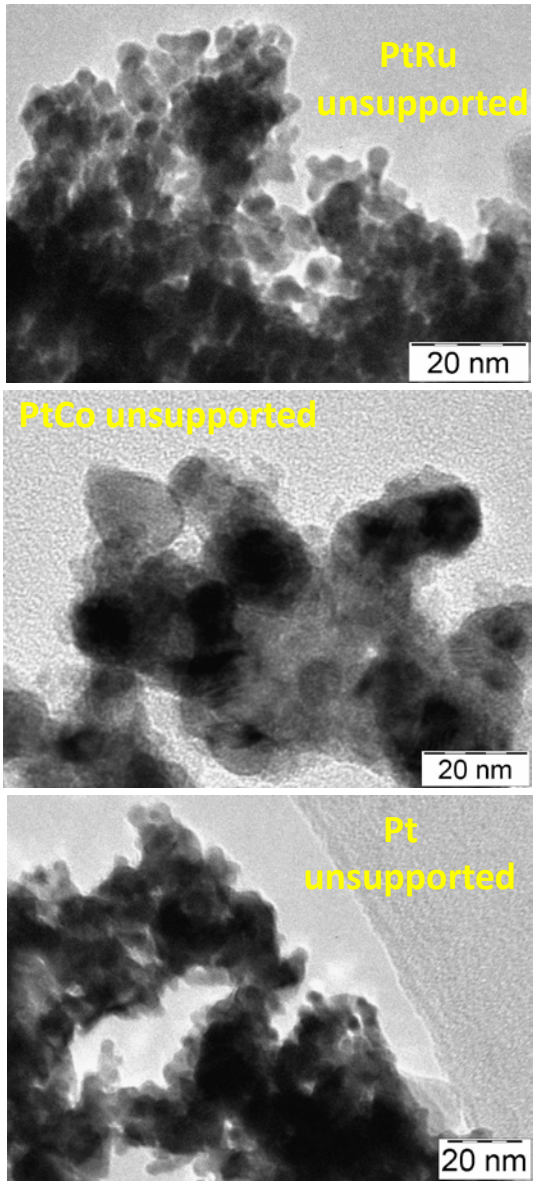

Fig. 26. High magnification TEM micrographs of the recombination /oxidation catalysts.

4.2.2 Assessment of the Pt-based catalysts for the hydrogen oxidation/ recombination in the gas-phase

The PtCo catalyst showed excellent recombination properties and it was selected for further assessment in the electrolysis cell. In fact, in the packed bed catalytic reactor, when hydrogen was fed at 4% in an oxygen stream (flammability limit), 99.5% of the total H_2 content was immediately converted to water thus avoiding safety issues. Thus, since 99.5% of H_2 was converted at the PtCo catalyst, this was corresponding in our experiments to 0.02 % residual H_2 (4%·99.5%). Moreover, the dynamic H_2 conversion response and the conversion rate under a steady-state regime remained optimal with the number of cycles (Fig. 27).

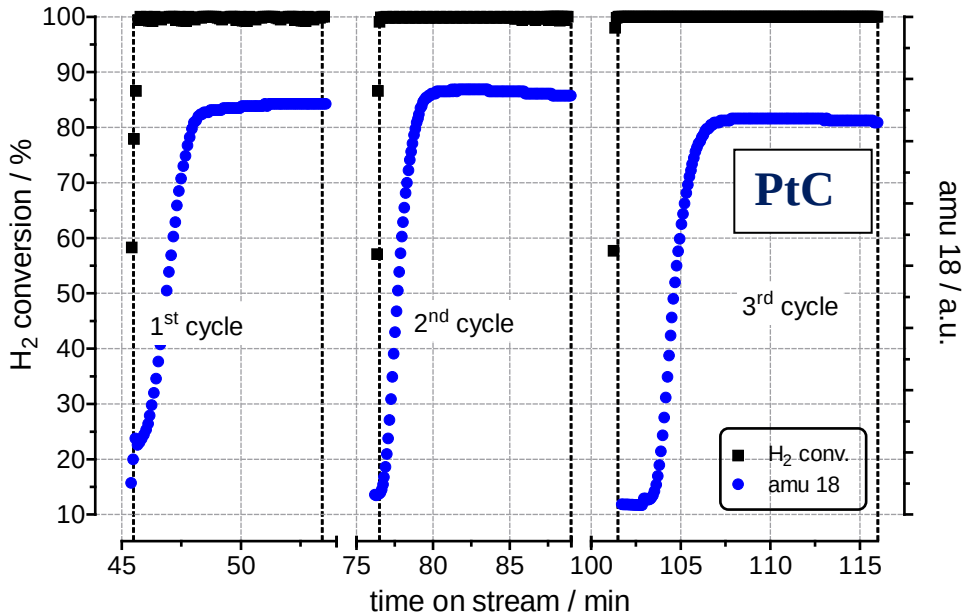

Fig. 27. Hydrogen conversion and water formation (H_2O = 18 amu-atomic mass unit) as a function of time at PtCo in a packed-bed catalytic reactor upon 4% vol. H_2 feed in a pure oxygen stream (three cycles). In each cycle, the catalyst was exposed to pure oxygen before feeding the 4% vol. H_2 – 96 % vol. O_2 mixture

On the contrary, the H_2 conversion was relatively poor for the PtRu 60:40 alloy compared to the PtCo system and the recombination performance significantly decreased with the number of cycles (Fig. 28). The H_2 conversion achieved with the PtRu 75:25 catalyst (Fig. 29) was higher than that obtained with the PtRu 60:40 but lower than the PtCo 75:25, especially after some cycles. This clearly indicates that the Ru addition to Pt is not favourable for the recombination process.

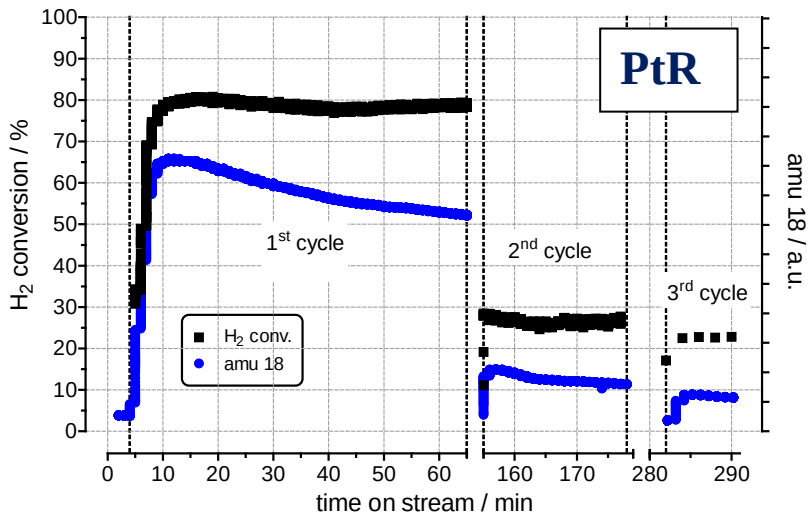

Fig. 28. Hydrogen conversion and water formation (H_2O = 18 amu-atomic mass unit) as a function of time at PtRu in a packed-bed catalytic reactor upon 4% vol. H_2 feed in a pure oxygen stream (three cycles). In each cycle, the catalyst was exposed to pure oxygen before feeding the 4 % vol. H_2 – 96 % vol. O_2 mixture.

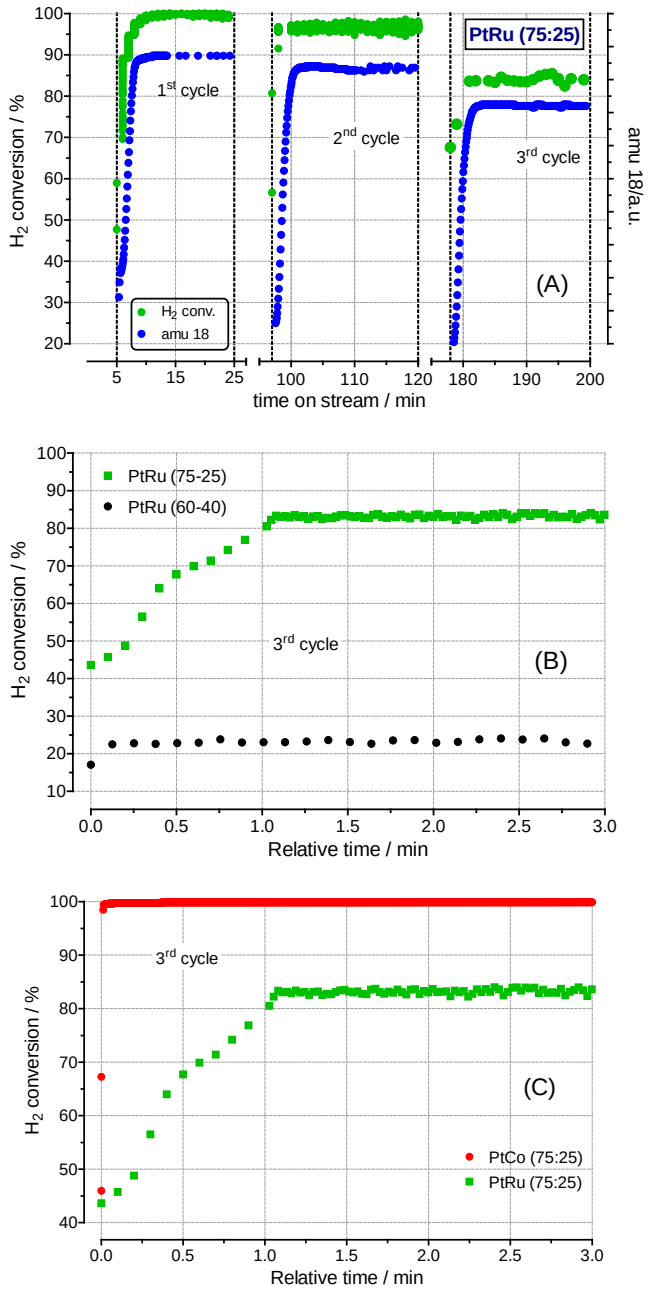

Fig. 29. (A) Hydrogen conversion and water formation (H_2O = 18 amu-atomic mass unit) as a function of time over a PtRu (75:25 at.) catalyst in a packed-bed catalytic reactor upon 4% vol. H_2 feed in a pure oxygen stream (three cycles). In each cycle, the catalyst was exposed to pure oxygen before feeding with the 4 % vol. H2 – 96 % vol. O_2 mixture. (B) Comparison of H_2 conversion response versus time for PtRu (75:25 at.) and PtRu (60:40 at.) catalysts after three cycles. (C) Comparison of H_2 conversion response versus time for PtRu (75:25 at.) and PtCo (75:25 at.) catalysts after three cycles.

These results are essentially ascribed to a chemisorption of oxygen on the Ru sites. Water is formed during this process. According to the well-known water displacement effect on the surface of the PtRu, this catalyst favours the surface uptake of oxygen species instead of adsorbed hydrogen intermediates. This process is well-known in aqueous solutions where formation of Ru-OH and Pt-OH species instead of Pt-H occurs on PtRu. This is favourable for the electro-oxidation of alcohols and CO in fuel cells but it reduces the reaction kinetics for H_2 oxidation. As matter of evidence, cyclic voltammetry analysis of PtRu catalysts

in the "so-called" hydrogen region does not provide a clear evidence of the Pt-H peaks because of the strong overlapping with the adsorbed OH species. This phenomenon does not occur in the cyclic voltammetry analysis of PtCo where the under-potential hydrogen adsorption peaks are well observed. The recombination performance of the Pt black catalyst was similar to that of the PtCo (Fig. 30a) even if the dynamic response appeared slower (Fig. 30b).

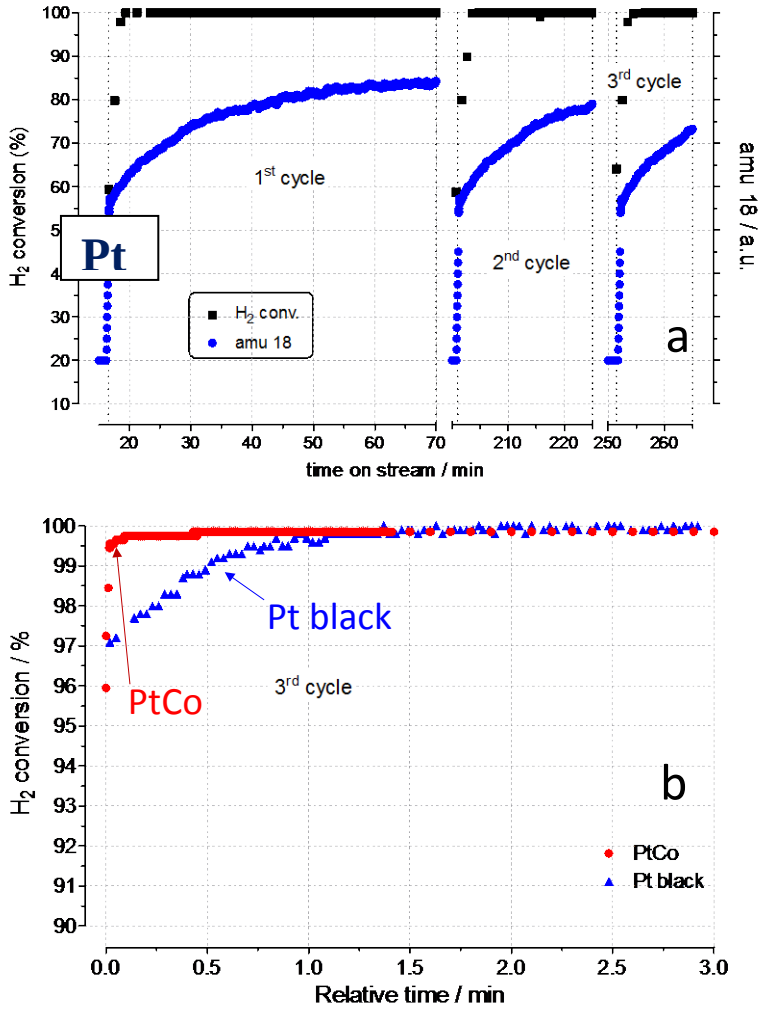

Fig. 30. a) Hydrogen conversion and water formation (H_2O = 18 amu-atomic mass unit) as a function of time at Pt black in a packed-bed catalytic reactor upon 4% vol. H_2 feed in a pure oxygen stream. In each cycle, the catalyst was exposed to pure oxygen before feeding the 4 % vol. H_2 – 96 % vol. O_2 mixture. b) Comparison of H_2 conversion response versus time for PtCo and Pt black catalytic systems after three cycles.

In order to understand if the PtCo was equally active for the recombination process in the liquid phase, a specific experiment was carried out by feeding the packed-bed reactor with a humidified inert gas to have the catalyst completely wetted on the surface. Thereafter, the reactor was fed with dry oxygen and subsequently with 4% vol. H_2 in O_2 stream. The subsequent cycles were carried out with dry gases as in the experiments discussed above. The H_2 conversion for the wet PtCo catalyst, at the beginning of the experiment, was substantially lower (50%) than that observed in the gas-phase (Fig. 31). However, during the first cycle, the H_2 conversion progressively increased as the result of a gradual catalyst drying, finally reaching an almost complete conversion after ca. 50 min on stream (Fig. 31). In the next cycle, the PtCo catalyst exhibited again very good recombination properties, being the hydrogen content immediately

converted to water without showing significant differences (see for comparison Fig. 27) in the third cycle. This experiment clearly indicates that the activity of the PtCo catalyst for recombination of H_2 and O_2 into water is much less efficient in the liquid phase than in the gas phase.

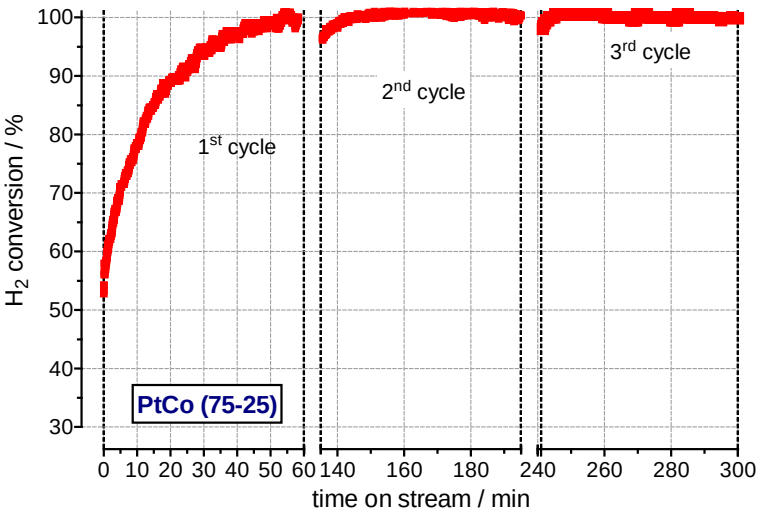

Fig. 31. Hydrogen conversion as a function of time over the PtCo (75:25) sample in a packed-bed catalytic reactor upon 4% vol. H_2 feed in a pure oxygen stream. Preliminarily, the catalyst was completely wetted under a flow of nitrogen carrier saturated with distilled water through a bubbler kept at 60°C by a thermostatic bath (Julabo F12-ED, USA), to get a water vapor pressure of 0.196 atm at a weight hourly space velocity (WGSV) of 1 $gH_2O/gcat/h$. Before feeding the dry 4% vol. H_2 in O_2 stream, the catalyst was exposed to a flow of pure (dry) oxygen. Before each new cycle with 4% vol. H_2 in O_2, the catalyst was exposed again to a flow of pure oxygen.

4.2.3 Surface characterisation of the Pt-based catalysts

The different catalysts (excluding the PtRu 3:1) were also characterised in terms of surface properties by X-ray photoelectron spectroscopy. By comparing the Pt 4f photoelectron peaks of the three catalysts (Fig. 32), it is evident that the sample characterised by a larger fraction of metallic platinum on the surface is the PtCo catalyst. The Pt $4f_{7/2}$ peak occurs at 71.30 eV for PtCo, 71.40 eV for Pt black and 72.1 eV for PtRu 60:40. The broadening and shift to higher binding energy of the Pt $4f_{7/2}$ peak together with the peculiar shape of the overall Pt4f profile for the PtRu catalyst (the intensity ratio between $Pt4f_{7/2}$ and $Pt4f_{5/2}$ should be 4:3 in a pure Pt metal) reveal the presence of a significant fraction of oxidised species in this sample. This in part occurs also in the Pt black catalyst, even if in a much lesser extent, compared to PtRu. Such evidences were confirmed by peak deconvolution analysis (Fig. 33). The concentration of oxidised species (Pt^{2+} and Pt^{4+}) was 69 % in the PtRu catalyst, 37% in the Pt black and 25% in the PtCo bimetallic alloy (Table 1).

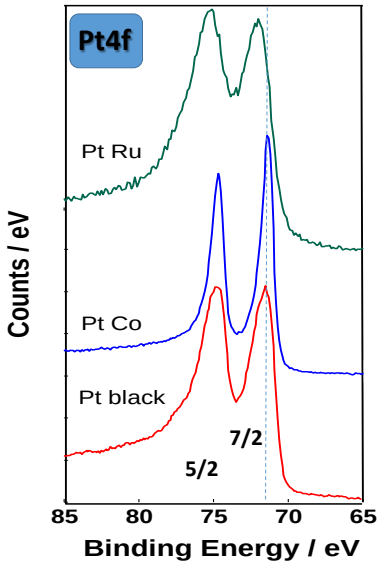

Fig. 32. High resolution X-ray photoelectron spectra of the Pt4f region of the recombination/hydrogen electro-oxidation catalysts

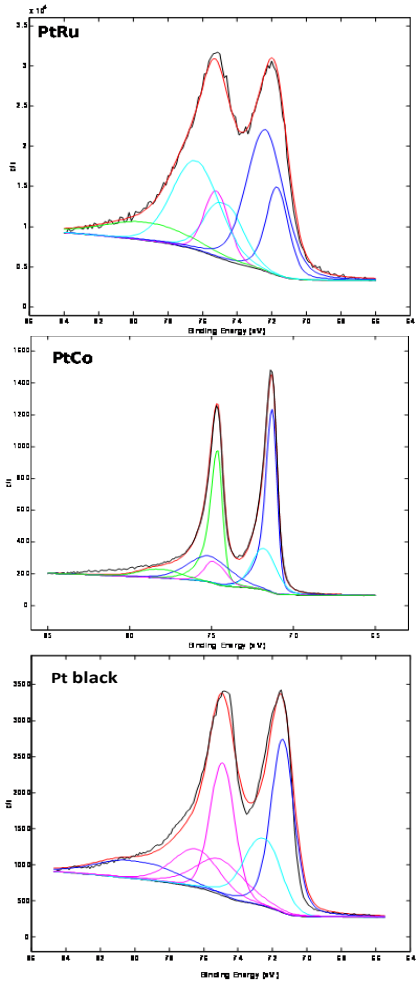

Fig. 33. Deconvoluted XP-spectra of the Pt4f signal in the unsupported catalysts.

Table 1. Binding energies and relative intensities for the different species from curve fitted XPS spectra in the various unsupported Pt catalysts

PtRu	***Binding energy Pt4f/7/2 eV***	***Relative peak area %***	***Assignment***
	71.70	**31.0**	**Pt°**
	72.38	**49.5**	**PtO**
	74.65	**19.5**	**PtO_2**
PtCo			
	71.30	**74.7**	**Pt°**
	71.79	**16.9**	**$Pt(OH)_2$**
	74.65	**8.4**	**PtO2**
Pt black			
	71.40	**62.7**	**Pt°**
	72.44	**24.4**	**PtO**
	74.90	**12.8**	**PtO_2**

Despite the fact that the PtCo catalyst was pre-leached in $HClO_4$ as final preparation step, the XP-survey spectrum shows the presence of both Pt and Co on the surface with modest occurrence of carbon and oxygen from adsorbed adventitious species (Fig. 34). O1s and C1s signals essentially derive from adsorbed organic species as confirmed by their significant reduction after a very mild sputtering of 10 min with Ar^+ ions (Fig. 35). The presence of Co in the outermost layers indicates a strong interaction with Pt causing acharge transfer which allows keeping Pt sites mostly in a reduced state.
According to these evidences and the gas-phase catalytic results, PtRu and Pt black catalysts were excluded from a further assessment in the electrochemical cell in favour of the PtCo system.

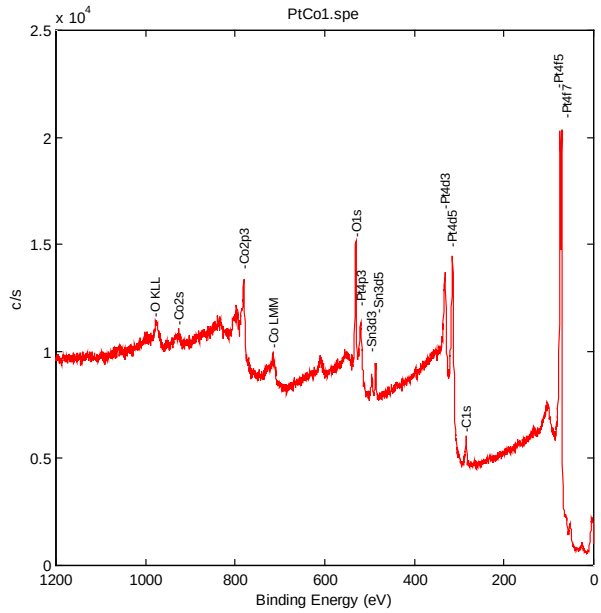

Fig. 34. XPS survey spectrum of the unsupported PtCo recombination/ hydrogen electro-oxidation catalysts.

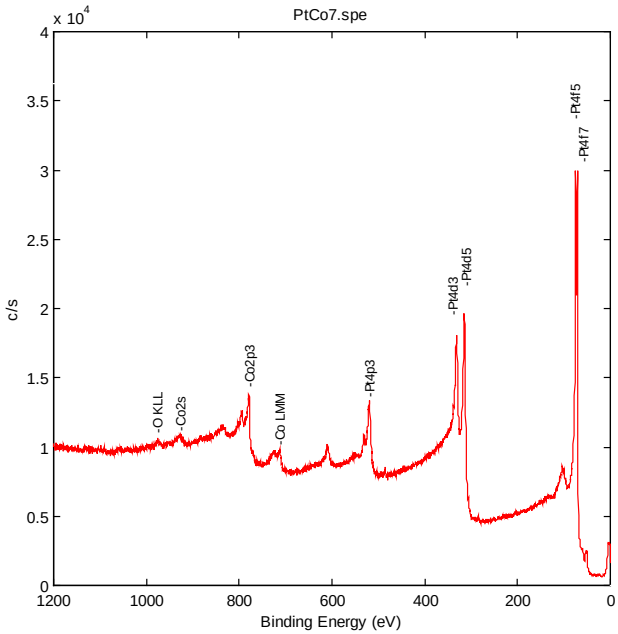

Fig. 35. XPS survey spectrum of the unsupported PtCo recombination/ hydrogen electro-oxidation catalyst after 10 min sputtering with Ar+ ions at 5 kV.

4.2.4 Single cell electrochemical assessment of a Pt-Co alloy for the hydrogen oxidation at the anode compartment of a PEM electrolysis cell

A comparison of the cross-sections of the membrane-electrode assemblies for the MEAs with and without the Pt-Co oxidation catalyst at the anode is shown in Figure 36. The anode catalyst appears much thinner and less regular than the cathode catalyst as consequence of the much larger density and significantly lower surface area of IrRuOx (150 m^2/g) compared to Ketjenblack® carbon (about 900 m^2/g) in 30% Pt/C (Fig. 36a). In the case of the modified MEA, a 0.1 mg PtCo cm^{-2} was integrated in the anode in between the membrane and the IrRuOx catalyst (Fig. 36b) by using a spray coating technique. An analysis at higher magnification of the interface between the membrane and

the dual-layer anode allows identifying the PtCo oxidation layer (Fig. 36c). This is very thin (about 4 microns) due to the high mass density of this unsupported catalyst. A good adhesion of the dual layer anode to the membrane is also observed (Fig. 36b-c).

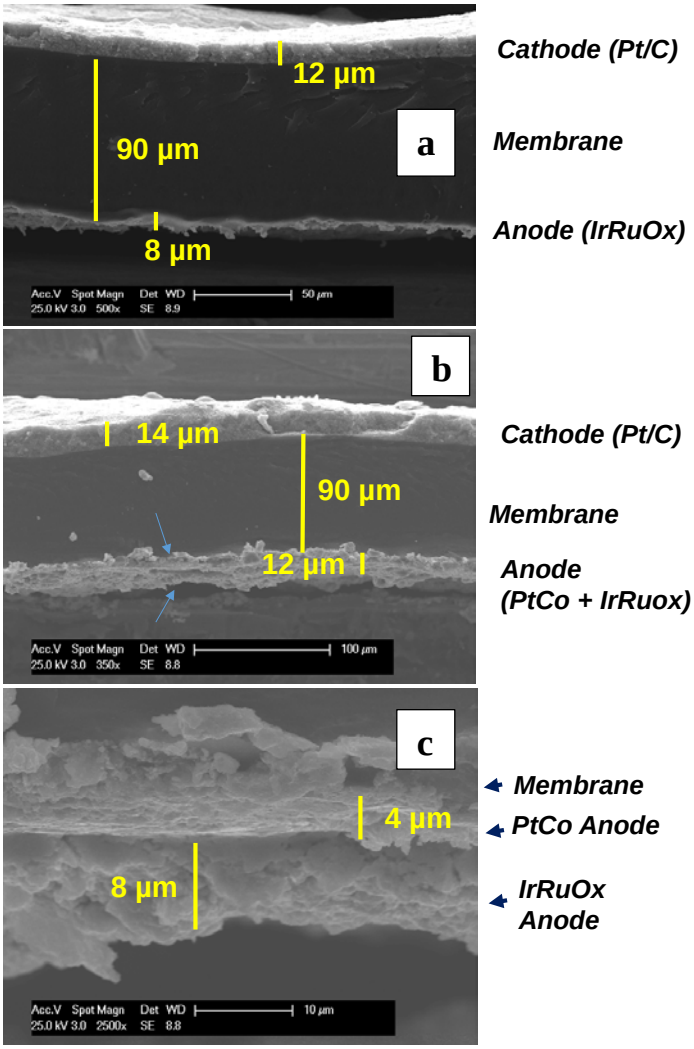

Fig. 36. Scanning electron micrographs of the MEAs (a) without and (b) with the PtCo hydrogen electro-oxidation catalysts; (c) magnification of the dual-layer (PtCo-IrRuOx) anode.

Single cell polarisation measurements at almost ambient pressure (1 bar differential pressure) of bare and PtCo-modified MEAs showed a slightly better performance of the cell containing the Pt-Co hydrogen oxidation catalyst showing about 100 mV lower cell voltage in almost all the overall range of current density (Fig. 37a). In particular, the enhanced performance was more evident at lower current densities in the activation-controlled region. This could be probably due to both the enhanced oxygen evolution (although Pt is less performing than IrOx for oxygen evolution, the additional Pt catalyst layer produces some effect being about 25% of the overall anode catalyst) and the oxidation of the permeated hydrogen. The latter process is very fast on Pt at high potentials. Thus, part of the permeated hydrogen was very likely oxidised to H^+ ions in the acidic environment at the PtCo catalyst. The formed protons back diffused to the cathode where they were reduced again to molecular hydrogen. This parasitic process does not contribute to the final amount of produced hydrogen in the outlet stream of the electrolyser; however, it affects the polarisation curve causing a depolarisation effect by means of such internal parasitic current.

Interestingly, when a differential pressure of 20 bars is applied between the cathode and anode (pressurised hydrogen, 20 bar gauge pressure; unpressurised oxygen, ambient pressure), the difference between the polarisation characteristics of the two MEAs is less relevant (Fig. 37b). The cell voltage of the PtCo - modified MEA is 30 mV lower than the bare MEA up to about 2 A cm^{-2}. The performance of these MEAs is similar at very high current density (Fig. 37b). Whereas the catalytic effect of PtCo is evident only in the low current density region.

There are some relevant aspects in the polarisation curves at 20 bar (Fig. 37b) that require a specific discussion. At low current density, an upward shift of the cell voltage for the curves at 20 bar (Fig. 37b) compared to the experiment at ambient pressure (Fig. 37a) is observed. This occurs because of a positive shift with the pressure of the reversible potential for water splitting according to the Nernst law. In addition, a flattening effect for the polarisation curves at 20 bar is observed at high current density (Fig. 37b). There are essentially two effects causing such peculiar behaviour. First, the water temperature is controlled at the cell inlet by a thermostat and this is assumed as the nominal cell temperature. During the pseudo-steady state polarisation measurements at high current density (data are collected when the cell performance stabilizes), there is an internal increase of the local temperature that is caused by the exothermic electrolysis reaction at potentials well above the thermoneutral potential. In effect, an increase of cell temperature (some degrees Celsius) is recorded for the outlet water during operation at high current density. This causes a decrease of the cell potential because both the membrane conductivity and the reaction kinetics are significantly enhanced by the increase of internal temperature. The low water flow rate used in our experiments does not allow to efficiently extracting the produced heat. A second effect is due to the formation of finer hydrogen bubbles at high pressure reducing the mass transport constraints at high current density. Thus, both the increase of the local temperature (increase of membrane conductivity and reaction kinetics) and the decrease of mass transport constraints, under high operating pressure, produce a decrease of cell voltage at high current density that is counteracted by the increase of ohmic drop with the current. The balance between these two opposite effects results in a flattening of the cell potential vs. current density profile in the high current density region compared to low operating currents. These aspects are also investigated using electrochemical impedance spectroscopy (see below).

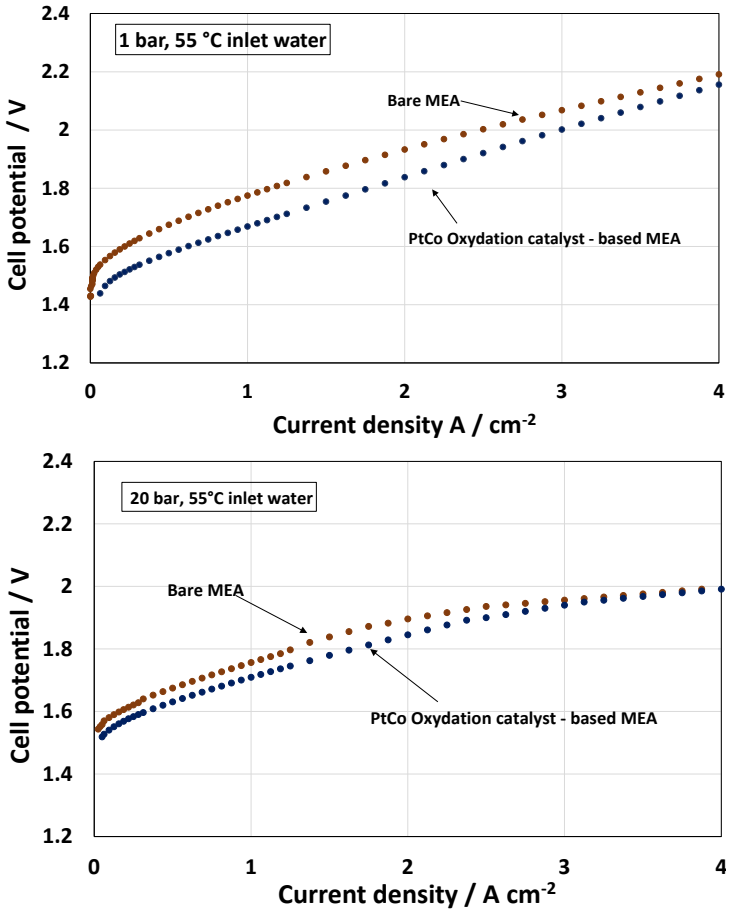

Fig. 37. Electrolysis polarization curves for the bare MEA and the MEA containing the PtCo oxidation catalyst at (a) 1 bar and (b) 20 bar differential pressure, at a constant water inlet temperature of 55°C.

Considering that the thermoneutral potential is about 1.5 V under such conditions, a voltage efficiency of 77% is achieved at 3 A cm^{-2} and 20 bar. It is interesting to note that at high pressure the polarisation curves for the bare and PtCo-based MEAs overlap at high current densities (Fig. 37b). This despite the fact that the permeated hydrogen is oxidised at the PtCo anode contributing in principle to the overall electrochemical reaction rate. However, at high overpotentials, also O_2 evolution is greatly enhanced. Under such conditions, the use of the additional PtCo catalytic layer does not produce a positive effect on the electrochemical reaction rate since the IrRuOx layer where oxygen evolution occurs is not in contact with the membrane. Usually, an intimate contact between IrRuOx and membrane favours the oxygen evolution process.

The measurements of the hydrogen gas concentration in the oxygen stream (anode) at ambient pressure (Fig. 38a), clearly show a relevant decrease of the hydrogen content in the overall range of current densities in the presence of a PtCo catalyst. The effect appears more relevant at the low operating current densities where a mitigation action is more important. At ambient pressure, there is almost 50% reduction of the H_2 concentration in oxygen in a wide range of current densities. In particular, at the lowest operating current density (0.15 A cm^{-2}) and at ambient pressure, the conversion of the permeated H_2 was about 46%. This is however substantially lower than that observed for same PtCo catalyst in the gas-phase in the packed-bed reactor (99.5%). Such relevant difference could be related to the different operating conditions, in particular liquid vs. gas-phase

operation (a substantial decrease of conversion was observed upon feeding water vapour in the packed bed reactor), or to a different reaction mechanism. This could be essentially based on the electrochemical oxidation of permeated H_2 to protons instead of H_2 conversion to water by effect of the evolved O_2. The electrochemical oxidation of H_2 should be very efficient at high potentials on metallic surfaces but the surface of the PtCo catalyst is very likely oxidised under electrolysis conditions with a consequent decrease of activity. On the other hand, in the gas phase experiments, pure oxygen was fed for more than 0.5 h, in each cycle, before hydrogen was injected into the O_2 stream. Thus, a chemical oxidation of the catalyst surface could have also occurred in the packed bed reactor. The lower occurrence of oxidised species on the surface of PtCo, evidenced by the XPS analysis, produces the best recombination activity among the investigated catalysts.

The reduction of the H_2 concentration in the oxygen stream is also relevant at 20 bar (Fig. 38b) even if it is less significant compared to what observed at ambient pressure. Probably, due to the thin unsupported PtCo catalyst layer over the membrane, the occurrence of preferential pathways for hydrogen permeation may occur under high differential pressure operation. However, the reduction of the hydrogen content in the anode stream appears similar at both operating pressures at least in terms of absolute values (Figs. 38a-b).

It is important to consider that, the excellent capability of the PtCo to act as recombination catalyst in the gas catalytic process was in part favoured by the presence of a thick and dense catalytic layer in the packed-bed reactor. Unfortunately, the need to reduce the Pt content in the electrochemical cell does not allow using a thick PtCo layer in the electrolysis MEA. The trade-off between the enhancement of the hydrogen production rate in the electrolysis system using a thin membrane and the increase of catalyst cost contribution by effect of the additional PtCo oxidation catalyst layer needs to be investigated more in-depth. However, for the present 90-µm membrane, the addition of just 0.1 mg cm^{-2} of PtCo hydrogen oxidation catalyst produces a decrease of the concentration of hydrogen in the oxygen stream well below the flammability limit of 4% also at a current density of 0.15 A cm^{-2}. Considering a nominal operating current density of 3-4 A cm^{-2} for this system, the PtCo hydrogen oxidation catalyst allows to extend the minimum partial load operation down to 5% (or less); whereas, nominal operating current is usually much lower than 4 A cm^{-2} for conventional systems and usually they do not allow partial load operation below 20% or 0.3 A cm^{-2}. It is clarified that minimum partial load also depends on the system's H_2 pressure. At pressures higher than 20 bar, the minimum percent of partial load may be higher.

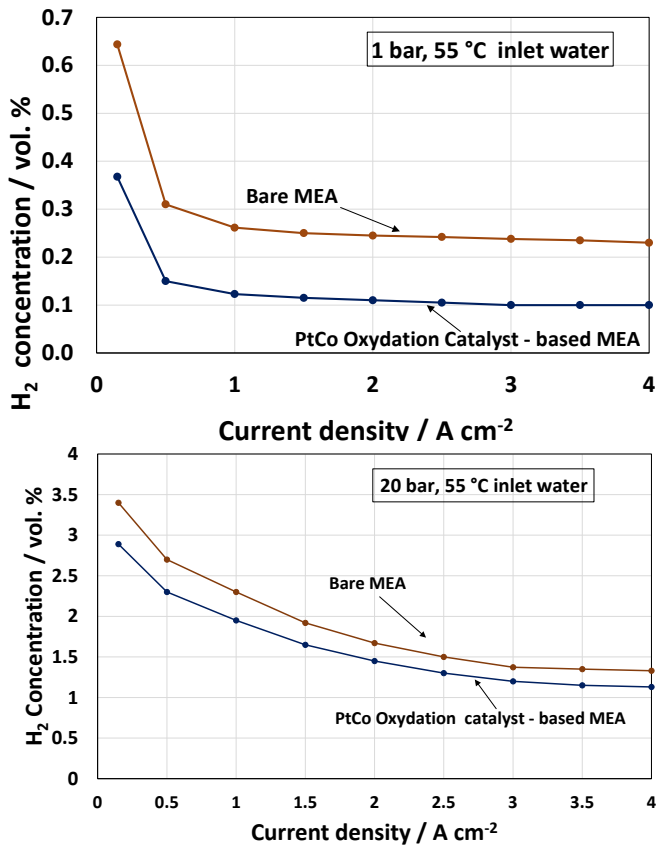

Fig. 38. Hydrogen fraction in the outlet anode stream at various current densities for the bare MEA and the MEA containing the PtCo oxidation catalyst at (a) 1 bar and (b) 20 bar differential pressure, at a constant water inlet temperature of 55°C.

The equivalent current density for the hydrogen permeation rate into the anodic outlet stream was estimated, at different operating electrolysis current densities, from the measured H_2 concentration in the anode stream and the oxygen production rate according to the following formulas:

$$C_{H_2} = \frac{mol_{H_2}^{permeated}}{mol_{H_2}^{permeated} + mol_{O_2}^{evolved}}; \quad (1)$$

$$I_{H_2}^{permeated} = 2 \cdot F \cdot mol_{H_2}^{permeated}; \quad \text{Faraday's law} \quad (2)$$

Where C_{H_2} is the experimentally determined concentration of hydrogen in the outlet anode stream; $mol_{O_2}^{evolved}$ are the number of evolved oxygen moles per unit of time; $mol_{H_2}^{permeated}$ are the calculated number of hydrogen moles per unit of time released into the anodic outlet stream; $I_{H_2}^{permeated}$ is the equivalent current density for the hydrogen permeation rate, 2 is the number of electrons exchanged during the oxidation of one hydrogen molecule and F is the Faraday's constant. This calculation neglects the oxygen cross-over to the cathode that in our high differential pressure experiments (hydrogen pressurised at 20 bar, non-pressurised oxygen) is relatively low (<1%) compared to the overall produced oxygen. This is confirmed by the comparison of the amount of oxygen evolved at the anode and the nominal oxygen production calculated from the Faraday's law at specific current densities.

The equivalent current density for the hydrogen permeation into the outlet anode stream, at various electrolysis current densities, for the bare MEA and the MEA containing the PtCo oxidation catalyst, at 1 bar and 20 bar differential pressures, is shown in Fig. 39a-b. It is observed that the hydrogen

permeation rate increases linearly especially at high operating current densities (Fig. 39 a-b). This permeation process is particularly related to the oversaturation of hydrogen in the cathode catalytic layer. The oversaturation increases proportionally with the electrolysis current density. At almost ambient pressure and very low current densities, the diffusion process may be essentially driven by the concentration gradient. The slope of the curve is lower under such conditions (Fig. 39a).
When the differential pressure was increased at 20 bar (Fig. 39b), the permeation rate was significantly higher than at ambient pressure. In this case, the permeation rate also increased linearly with the current density but according to two different slopes. The slope was higher at low current density (Fig. 39b). According to the high pressure conditions, a supersaturation of the cathode layer with H_2 is also occurring in this range and hydrogen permeation at low current densities is facilitated by a lower oxygen production at the anode side. Of course, this phenomenon is critical for the system safety. The observed hydrogen permeation rate into the anode outlet decreases in the presence of the PtCo catalyst, at both pressures (Fig. 39a-b), as this catalyst converts a fraction of the hydrogen permeated through the membrane to protons.

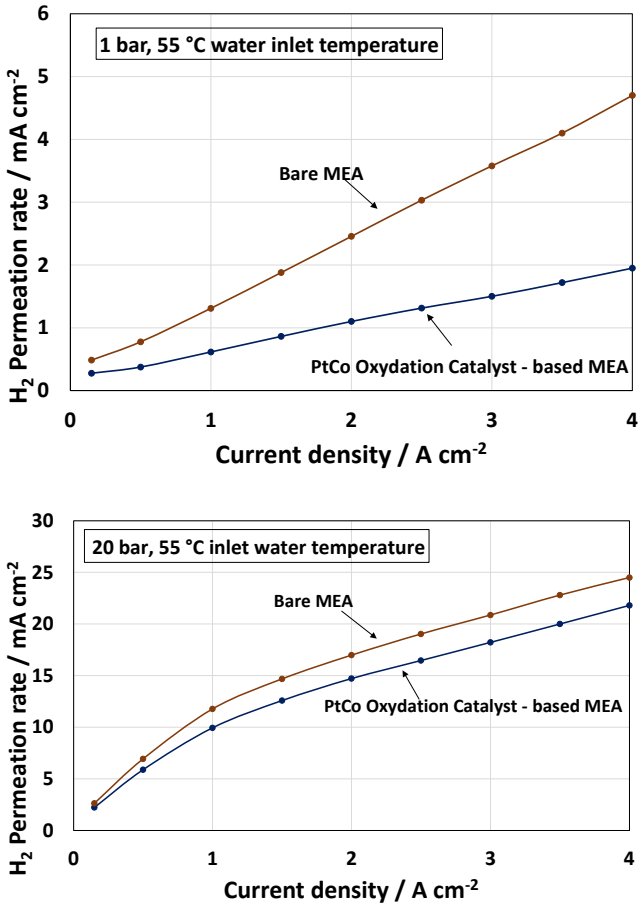

Fig. 39. Equivalent current density for the hydrogen fraction in the outlet anode stream at various electrolysis current densities for the bare MEA and the MEA containing the PtCo oxidation catalyst at (a) 1 bar and (b) 20 bar differential pressure, at a constant water inlet temperature of 55°C.

Faradaic efficiency was estimated from the hydrogen flow rate after a cryogenic drying (Fig. 42). At 20 bar, the faradaic efficiency was about 99% in a wide range of current densities from 0.5 to 3 A cm^{-2} for both MEAs. This high faradaic efficiency, achieved in the presence of a relatively thin membrane (90 µm), clearly shows that the problem of hydrogen permeation into the anode is not affecting significantly the electrolysis efficiency but mainly the system safety especially under low current density operation.

The polarisation curves, recorded at different differential pressures, are compared in Fig. 40a. As discussed above, an increase of the cell voltage with the increase of pressure is observed at low current densities. Instead, at large current densities, the internal increase of temperature caused by a poor heat exchange, which appears more relevant under pressure, and the decrease of the size of gas bubbles with pressure play an important role. Practically, the system efficiency at high current density is improved by the increase of temperature and pressure.
Also in the presence of PtCo, the hydrogen concentration increases significantly in the low current density range (Fig. 40b). However, the safety limit becomes critical at 20 bar for a current density lower than 0.15 A cm^{-2} (Fig. 40b). One can see that a further increase of the operating pressure is possible but the safety limit for the minimum operating current density will shift towards higher currents. In other words, electrolysis systems operating at very high pressure have a smaller partial load range. The rate of hydrogen permeation with the current density increases with the pressure (Fig.39). However, the hydrogen permeation in the outlet anode stream remains relatively low compared to the amount of hydrogen produced at the cathode for the present combination of PtCo oxidation catalyst and Aquivion® membrane (90 µm).

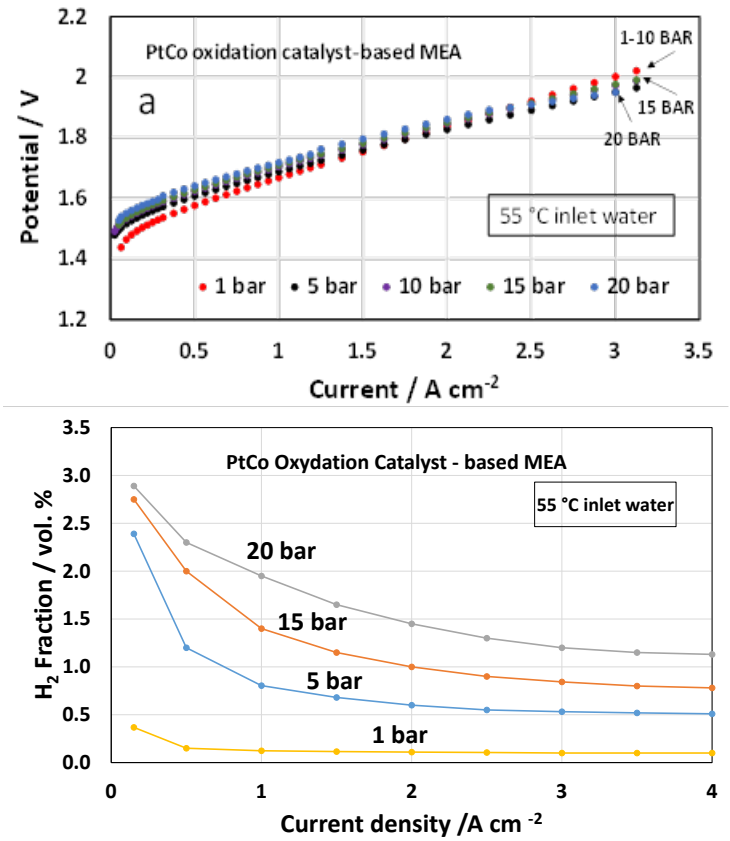

Fig. 40. Polarisation curves (a) and hydrogen fraction in the outlet anode stream (b), at different pressures, for the MEA containing the PtCo oxidation catalyst, at a constant water inlet temperature of 55°C.

The effect of the differential pressure was also investigated, under constant voltage efficiency conditions, by electrochemical impedance spectroscopy. Nyquist plots for the MEA containing the PtCo oxidation catalyst, obtained at 1.5 V and 1.8 V, at different pressures, are reported in Figs. 41a-b. This was useful to get insights about the limiting steps affecting the electrolyser operation in the activation-controlled region and at high current densities. At 1.5 V voltage (Fig. 41a), a single

semicircle is evident in the investigated frequency range. This is essentially related to the charge transfer process associated to the oxygen evolution reaction (rate determining step under these conditions). As discussed above, the reversible Nernst potential shifts positively with the increase of pressure. Thus, the effective applied overvoltage decreases with the increase of the operating pressure. For purely kinetic processes, the reaction rate (current density) and applied overpotential are directly related according to the Volmer-Butler equation. Thus, the increase of charge transfer resistance with the increase of pressure in this region (Fig. 41a) is essentially due to this effect.
Fig. 41b shows instead at 1.8 V a decrease of the overall differential resistance (low frequency intercept on the real axis) with pressure. Two semicircles are observed in these spectra. The high frequency semicircle is still related to the charge transfer process associated to the oxygen evolution reaction whereas the low frequency semicircle is very likely related to mass transport limitations. At the same pressure, the charge transfer process associated to the oxygen evolution is significantly lower at 1.8 V than at 1.5 V due to the effect of the different overpotential according to the Volmer-Butler equation (Fig. 41). However, the decrease of charge transfer resistance with pressure in the high current density region (1.8 V) is possibly related to a depolarisation effect caused by the hydrogen cross-over to the anode.
The decrease of the mass transfer resistance with pressure at low frequency is instead likely related to the formation of finer gas bubbles. Interestingly, at 1.8 V (Fig. 41b), there is a decrease of the series resistance (high frequency intercept on the real axis of the Nyquist plot) passing from almost ambient pressure to 20 bar differential pressure probably caused by an improved MEA compression.

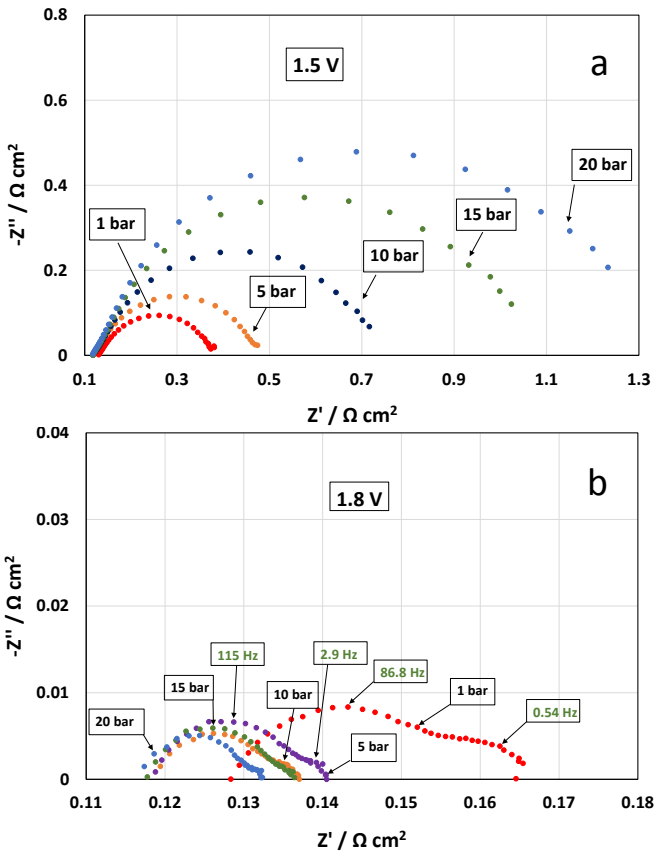

Fig. 41. Electrochemical impedance spectra, at 1.5 V (a) and 1.8 V (b), at different pressures, for the MEA containing the PtCo oxidation catalyst, at a constant water inlet temperature of 55°C

The depolarisation phenomena, observed in the presence of the PtCo catalyst, both in polarisation (Fig. 37) and impedance (Fig. 41) studies, together with the significantly lower H_2 conversion

recorded when the catalyst was in a wet state in the packed bed reactor (Fig. 31) would suggest a prevailing electrochemical oxidation mechanism for the permeated H_2 in the electrolysis cell. This can be in part due to the fact that the PtCo layer is coated directly on the membrane; thus, it is less exposed to the oxygen evolved at the IrRuOx layer that preferentially diffuses towards the titanium mesh backing layer.

The present approach can allow for the use of thinner membranes in electrolysis. A comparison of the H_2 concentration in the outlet anode stream for the present system with the literature results for conventional MEAs, based on much thicker membranes (170 µm, 230 µ) is shown in Fig. 42a-b. This comparison indicates a positive role of the PtCo catalyst especially in the low range of current density. For thick membrane based MEAs, there are not many literature data available for the hydrogen concentration in the anode stream at current densities higher than 2-3 A cm^{-2}. The reason is essentially due to the fact that the voltage efficiency for a thick membrane-based MEA is relatively low at high current density. This is due to the large ohmic drop. Thus, there is no interest in analysing the cell behaviour under conditions which are not of practical relevance. From the trend observed in Fig. 42, it may be possible that at very high current density, the concentration of hydrogen in the anode stream is lower for thick membranes compared to thin membranes even combined with a PtCo catalyst. However, this appears to be less relevant because the region where the role of the oxidation/ recombination catalyst is more important is that at low current densities.

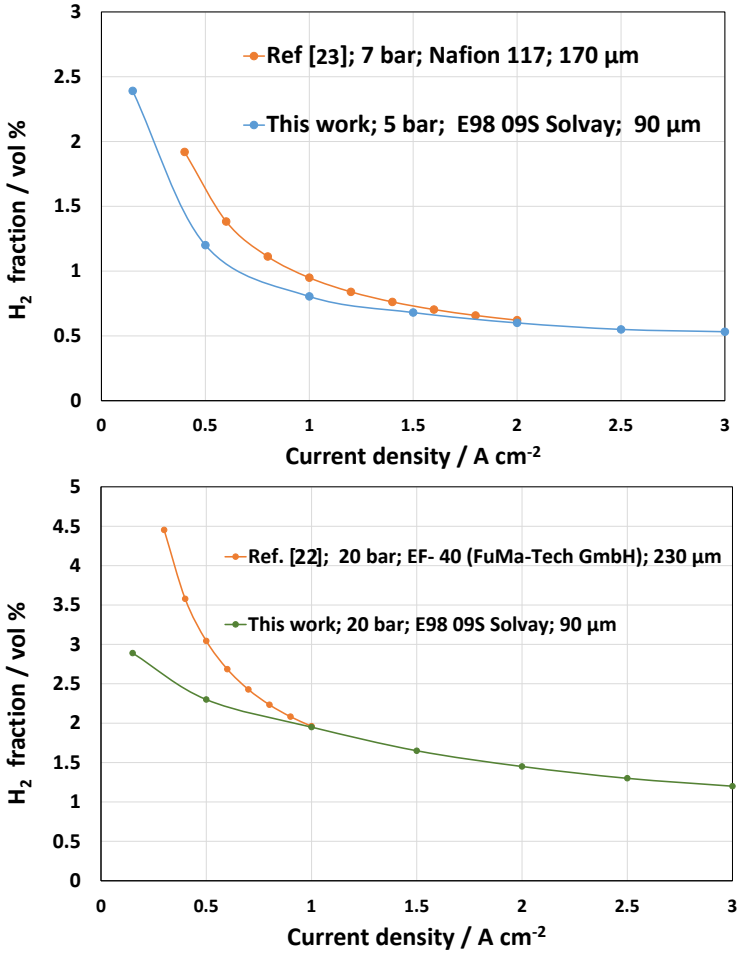

Fig. 42. Comparison of the H_2 concentration in the outlet anode stream for the present PtCo oxidation catalyst-modified MEA and the literature results for conventional MEAs based on thicker membranes

On the other hand, one may consider the opportunity to further decreasing the thickness of the membrane in the presence of the PtCo catalyst but this may require sacrificing in part the extension

of the partial load operating range compared to thick membranes. This would mean a less flexible system to cope with dynamic electricity production from renewable sources.
For the moment, the PtCo catalyst appears beneficial in terms of reduction of the hydrogen concentration in the anodic stream when it is combined with a membrane of proper thickness. The increased catalyst cost, due to the additional PtCo layer, is largely compensated by a significant increase of the hydrogen production rate (lower capital costs) at the same efficiency as consequence of the reduced ohmic losses associated to the thin membrane.

5. ELECTROCATALYSTS MEETING THE SPECIFICATIONS: ASSESSMENT OF PROJECT MILESTONE MS3

MS3 is combining three targets for the developed catalysts: low overpotentials, good stability, capability of reducing hydrogen concentration in oxygen by using a recombination catalyst under certain reference conditions.

MS3 -Advanced nanostructured anode catalysts; high surface area cathode catalysts supported on carbon nanofibers; efficient recombination catalysts

Means of verification:
-Reduced oxygen and hydrogen evolution overpotentials (< 200 mV and <50 mV IR-free at 4 A cm^{-2} with noble metal loading < 0.35 mg cm^{-2} and < 0.05 mg cm^{-2} respectively) and
- low degradation rate (<5% decrease in electrochemical surface area after a 2000 h durability test at 4 A cm^{-2});
- recombination catalyst producing relevant decrease of hydrogen concentration (<0.2 vol % H_2).

The results relevant to the achievement of this milestone are reported in the following.

To assess performance of anode and cathode catalysts, these were evaluated in MEAs in combination with Aquivion membrane and ionomer dispersions. Tests were carried out in complete electrolysis cells to determine the overall cell voltage and in symmetrical cells, in the hydrogen pumping mode to evaluate cathodic overpotential.

In the following we estimate the overpotentials with respect to the thermoneutral and reversible potential for water splitting. Usually the thermonutral potential is the correct option because the energy needed for water splitting include the reverible heat ($T\Delta S$). However, since some heat was externally supplied when the cell was operated at 90 °C (even if at 4 A cm^{-2} , due to the exothermic reaction, the supplied heat is very small), the effective thermodynamic potential for water splitting is in between these two parameters.

Thus, anode overpotential was thus determined at 4 A cm^{-2} from the difference:
$E_{cell} = E_{anode} + E_{cathode} + E_{tn}$
or
$E_{cell} = E_{anode} + E_{cathode} + E_{rev}$.

Where E_{tn} is the thermoneutral potential and E_{rev} is the reversible potential.

Ohmic drop was determined from ac-impedance measurements, reported and subtracted from the recorded overpotentials. Curves are reported as raw and IR-free. Anodic and cathodic overpotentials were determined at 90 °C.
All the potentials were corrected for the ohmic drop in order to separate the electrocatalyst contribution from the ohmic losses.

Total overpotential (anode + cathode) vs. E_{tn} (90°C)

Theoretically: E_{tn} + IR loss+ target overpotential =
1.47 V + (0.063 Ohm $cm^2 \cdot 4$ A cm^{-2}) + 0.25 V = 1.47 + 0.25 + 0.25 = 1.97 V @ 4 A cm^{-2}.
Recorded: 1.8 V/cell at 4 A cm^{-2} and 90°C: Overpotential = 1.8 - (1.47 + 0.25) = 80 mV
Total overpotential vs. E_{tn}= 80 mV
Target largely achieved (80 vs. 250 mV)

Total overpotential (anode + cathode) vs. E_{rev} (90°C)
Theoretically E_{rev} + IR_{loss}+ target overpotential =
1.23 V + (0.063 Ohm $cm^2 \cdot 4$ A cm^{-2}) + 0.25 V = 1.23 + 0.25 + 0.25 = 1.73 V @ 4 A cm^{-2}.
Recorded 1.8 V/cell at 4 A cm^{-2} and 90°C: Overpotential = 1.8 - (1.23+0.25) = 320 mV
Total overpotential vs. E_{rev}= 320 mV

Target not fully achieved (320 vs. 250 mV)

Reaction onset is in between E_{tn} and E_{rev} due to the internal/external supply of heat (90 °C and 4 A cm^{-2}). It could be appropriate to evaluate the overpotential vs. the onset potential for the reaction. This is about 1.359 V.

Also in this case:

Recorded: 1.8 V/cell at 4 A cm^{-2} and 90°C: Overpotential = 1.8 - (1.359 + 0.25) = 200 mV
Total overpotential vs. E_{tn}= 200 mV
Target achieved (209 vs. 250 mV)

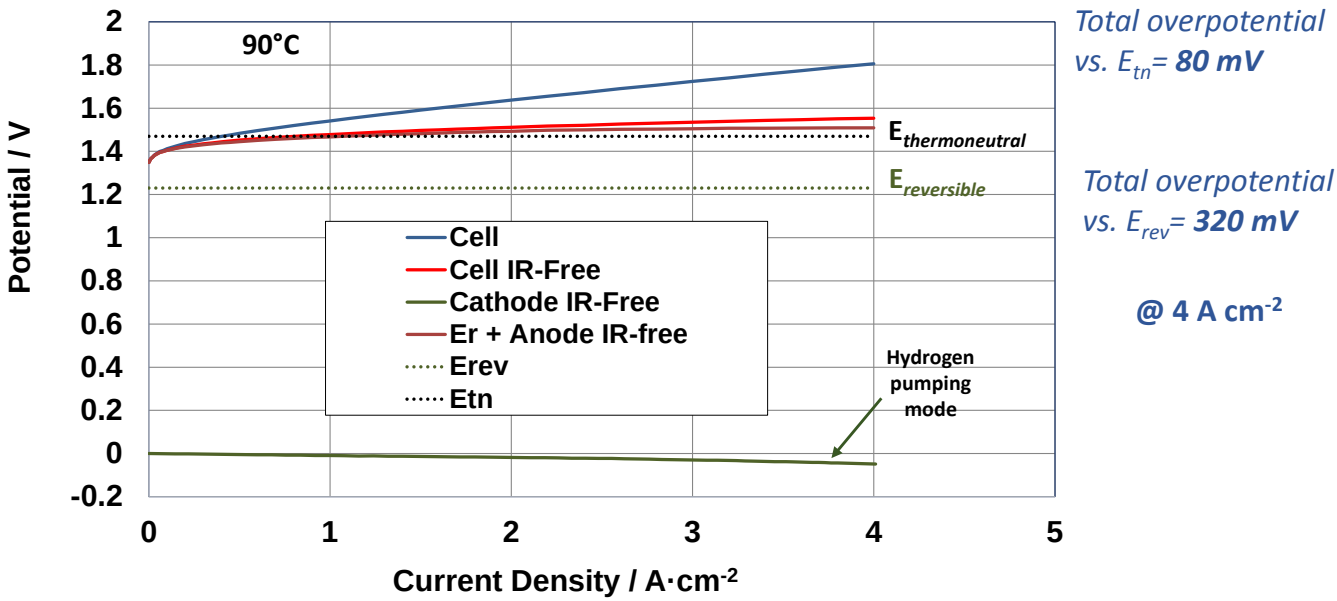

Fig. 43. Polarization curves of cell, anode and cathode overpotential at 90 °C

In Figure 43 the polarization curves relative to cell, anode e cathode overpotentials are reported. A hydrogen pumping mode was used to determine the cathode overpotential. The total overpotentials result 80 mV vs. E_{tn}, 209 mV vs. the onset potential for water splitting and 320 mV vs. E_{rev}, respectively.

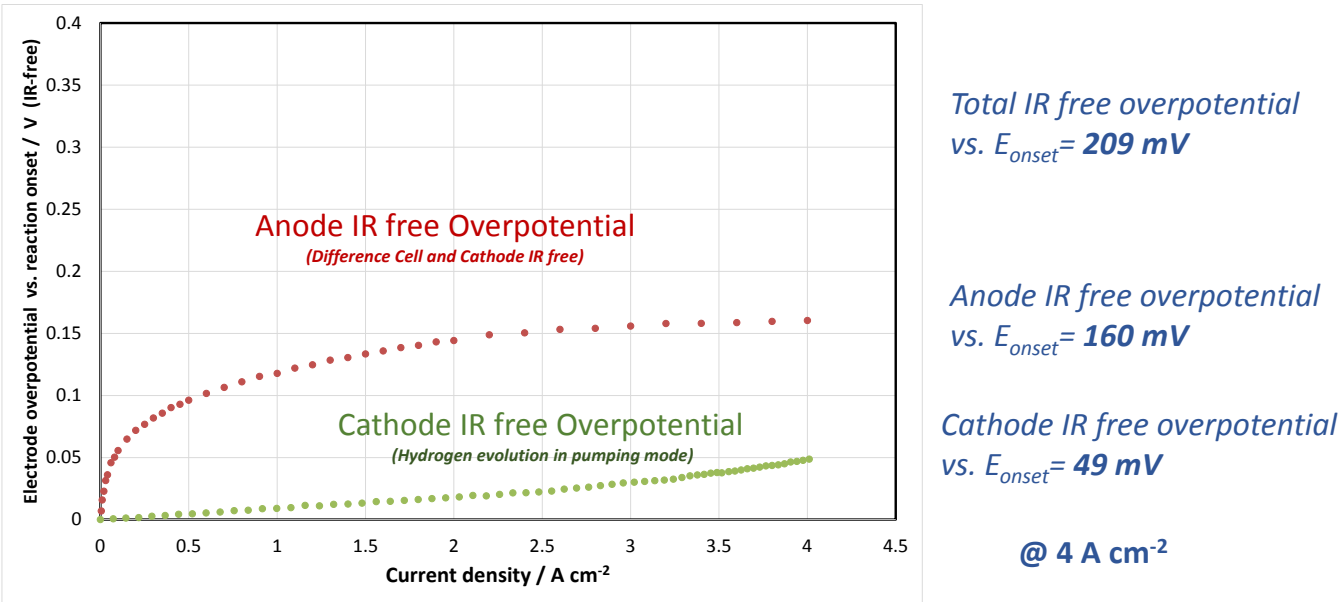

Fig. 44. Cathode and Anode IR free overpotential vs. reaction onset

The overall IR-free electrode overpotentials at 4 A cm^{-2} and at 90 °C amount to 209 mV with respect to a target of < 250 mV (49 mV cathode + 160 mV anode) . Thus, the part of MS3 relative to the

overpotential can be considered achieved (**MS3**: < 200mV for OER and 50mV for HER at 4 A cm^{-2} (Total Overpotential < 250 mV).

Concerning the part of MS3 relative to the hydrogen concentration < 0.2 vol % H_2 in O_2, Fig. 38 shows that while operating with the E98-09S Aquivion membrane, the H_2 concentration in O_2 decreases by about 40% in the presence of the PtCo recombination catalyst at ambient pressure and at a temperature of 55 °C with a concentration lower than 0.2 % H_2 in O_2 in the current density range from 0.5 to 4 A cm^{-2} i.e. in the load range from 10% to 100 %. Thus, the part of MS3 relative to the hydrogen concentration can be considered achieved even if further analysis at different temperatures including 90 °C is underway.

With regard to the catalyst stability, the part of MS3 relative to a decrease of surface area less than 5% after 2000h durability test at 4 A cm^{-2} is not yet addressed since the 2000 h durability experiment is still running; once completed an analysis of the surface area variation will be carried out.
However, as mentioned above the performance decay rate in Fig. 16 for the developed catalysts in the presence of the Aquivion® membrane E98-05S is corresponding to 4.4 µV/h when the last 1000 h are considered in the overall 2000 h durability test (almost 1900 h at 4 A cm^{-2}).
These results are promising and in line with MS7 milestone, even if achieved at the single cell level (not in the stack as required by MS7) and at 80 °C instead of 90 °C as indicated in the DoW.

However, these results indicate that the developed catalysts (the ones down-selected for the durability studies) may be appropriate for the large area MEAs to be tested in the stack configuration.

6. CONCLUSIONS

The activities described in this deliverable deal with workpackage WP4: Enhanced catalysts. WP4 aims essentially enhancing the stability, reduce the cost and increase the performance of polymer electrolyte membrane water electrolyser electrocatalysts.

The main approach for the anode catalyst were the improvement of the intrinsic activity and stability through tailoring anode catalyst surface chemistry, electronic effects and crystallographic orientation. The aim was to produce stable nanostructured solid solutions of Ir and Ru with a core-shell configuration consisting of Ir enrichment on the surface and optimised crystallographic orientation.

As for the anode catalyst, noble metal-based cathode catalysts was developed in order to provide corrosion resistance in acidic environment and appropriate catalytic activity for hydrogen evolution. The aim was to further reduce the cathode catalyst loading to less than 0.1-0.05 mg cm^{-2}, increase current density up to 4-8 A cm^{-2} while keeping the low overpotential characteristics of the hydrogen evolution process.

A Pt-Co alloy catalyst showed good H_2-O_2 recombination capability in the gas phase after exposure to 4% vol. H_2 in O_2; this was not the case of PtRu alloys. According to the XPS results, the recombination performance appears to be correlated with the capability of the PtCo alloy system to keep Pt sites in a reduced oxidation state compared to other Pt catalysts. For the PtCo system, during operation in the gas phase catalytic reactor, it was observed that about 99.5% of H_2 was immediately converted to water when it was fed at 4% vol. in the oxygen stream (lower flammability limit).

Integration of the PtCo alloy catalyst in the membrane-electrode assembly, in particular between the membrane and the IrRuOx anode catalyst, showed also good electrochemical performance for the oxidation of the permeated hydrogen. In this case, the mechanism mainly consisted in an electrochemical oxidation of the permeated H_2 to protons that were transported back to the cathode according to the electric field gradient effect. At the cathode, these ions were reduced again to molecular hydrogen. This parasitic current was not affecting much the faradaic efficiency of the system that remained larger than 99% in almost the overall range of operating current densities. The prevailing electrochemical oxidation mechanism for the permeated H_2 in the electrolysis cell is supported by the occurrence of relevant depolarisation phenomena in the presence of the PtCo catalyst. Moreover, a much lower recombination conversion was observed in the packed bed reactor with the PtCo catalyst in a wet state.

The H_2 concentration in the oxygen stream of the PEM electrolyser decreased significantly at all pressures in the presence of the PtCo catalyst. At 20 bar differential pressure, in the presence of PtCo, the hydrogen concentration in the anodic oxygen stream was well below the flammability limit also when the current density was as low as 0.15 A cm^{-2}. This corresponds to less than 5% partial load operation for the nominal current density of 4 A cm^{-2} for the present system compared to a minimum partial load of 20% for conventional electrolysis systems even if under different conditions. This characteristic provides better flexibility to cope with the dynamic behaviour of renewable power sources. The observed H_2 concentration in the oxygen stream for the present electrolysis system is lower than that reported in the literature for PEM electrolysis cells operating at both similar pressures and current densities in the presence of much thicker membranes-based electrolytes.

The investigation of anode and cathode overpotentials at 90 °C indicated an overall overpotential of 209 mV vs. the onset potential for water splitting. This was resulting from 160 mV overpotential for the oxygen evolution and 49 mV overpotential for hydrogen evolution processes, respectively. The recombination catalyst allowed to decrease the H_2 concentration in the oxygen stream to less than 0.2 % at 55 °C and 4 A cm^{-2} whereas the voltage degradation in a test of almost 2000 h at 4 A cm^{-2} was less than 5 µV (in the last 1000 h). All these results are in line with MS3 and MS7 milestones. A 2000 h test at 4 A cm^{-2} is underway. Once completed the analysis of the surface area loss will be determined and reported in D4.2.